Journal of Materials Chemistry A

ROYAL SOCIETY OF CHEMISTRY

PAPER

View Article Online
View Journal

Cite this: DOI: 10.1039/d1ta04252a

Perovskite Na-ion conductors developed from analogous $Li_{3x}La_{2/3-x}TiO_3$ (LLTO): chemo-mechanical and defect engineering†

Yu-Ying Lin, [ac] William J. Gustafson, [bc] Shannon E. Murray, [ac] Daniel P. Shoemaker, [ac] Elif Ertekin, [ac] Jessica A. Krogstad *[ac] and Nicola H. Perry *[ac]

Na-ion conducting solid electrolytes can enable both the enhanced safety profile of all-solid-state-batteries and the transition to an earth-abundant charge-carrier for large-scale stationary storage. In this work, we developed new perovskite-structured Na-ion conductors from the analogous fast Li-ion conducting $Li_{3x}La_{2/3-x}TiO_3$ (LLTO), testing strategies of chemo-mechanical and defect engineering. $Na_xLa_{2/3-1/3x}ZrO_3$ (NLZ) and $Na_xLa_{1/3-1/3x}Ba_{0.5}ZrO_3$ (NLBZ) were prepared using a modified Pechini method with varying initial stoichiometries and sintering temperatures. With the substitution of larger framework cations Zr^{4+} and Ba^{2+} on B- and A-sites respectively, NLZ and NLBZ both had larger lattice parameters compared to LLTO, in order to accommodate and potentially enhance the transport of larger Na ions. Additionally, we sought to introduce Na vacancies through (a) sub-stoichiometric Na : La ratios, (b) Na loss during sintering, and (c) donor doping with Nb. AC impedance spectroscopy and DC polarization experiments were performed on both $Na_{0.5}La_{0.5}ZrO_3$ and $Na_{0.25}La_{0.25}Ba_{0.5}ZrO_3$ in controlled gas environments (variable oxygen partial pressure, humidity) at elevated temperatures to quantify the contributions of various possible charge carriers (sodium ions, holes, electrons, oxygen ions, protons). Our results showed that the lattice-enlarged NLZ and NLBZ exhibited ~19× (conventional sintering)/49× (spark plasma sintering) and ~7× higher Na-ion conductivities, respectively, compared to unexpanded $Na_{0.42}La_{0.525}TiO_3$. Moreover, the Na-ion conductivity of $Na_{0.5}La_{0.5}ZrO_3$ is comparable with that of $NaNbO_3$, despite having half the carrier concentration. Additionally, more than 96% of the total conductivity in dry conditions was contributed by sodium ions for both compositions, with negligible electronic conductivity and little oxygen ion conductivity. We also identified factors that limited Na-ion transport: NLZ and NLBZ were both challenging to densify using conventional sintering without the loss of Na because of its volatility. With spark plasma sintering, higher density can be achieved. In addition, the NLZ perovskite phase appeared unable to accommodate significant Na deficiency, whereas NLBZ allowed some. Density functional theory calculations supported a thermodynamic limitation to creation of Na-deficient NLZ in favor of a pyrochlore-type phase. Humid environments generated different behavior: in $Na_{0.25}La_{0.25}Ba_{0.5}ZrO_3$, incorporated protons raised total conductivity, whereas in $Na_{0.5}La_{0.5}ZrO_3$, they lowered total conductivity. Ultimately, this systematic approach revealed both effective approaches and limitations to achieving super-ionic Na-ion conductivity, which may eventually be overcome through alternative processing routes.

Received 19th May 2021
Accepted 24th August 2021

DOI: 10.1039/d1ta04252a

rsc.li/materials-a

1 Introduction

Lithium-ion batteries have developed rapidly in the past few decades to support their use in a variety of applications, ranging from mobile devices to electric vehicles. However, the limited availability of lithium is causing a significant shift in interest towards new types of rechargeable batteries, such as sodium-based systems, because of their low cost and earth-abundance.[1] Furthermore, conventional liquid/polymer-based electrolytes raise safety and manufacturing concerns, owing to their flammability and thermal instability, limiting their application

[a]Department of Materials Science and Engineering, University of Illinois at Urbana-Champaign, IL, USA. E-mail: jakrogst@illinois.edu; nhperry@illinois.edu
[b]Department of Mechanical Science and Engineering, University of Illinois at Urbana-Champaign, IL, USA
[c]Materials Research Laboratory, University of Illinois at Urbana-Champaign, IL, USA

† Electronic supplementary information (ESI) available: Synchrotron XRD data for NLZ-N0.5-(1200C 6hr) and NLBZ-N0.25-(1200C 6hr). Measurements with different electrodes. More discussion on transference numbers of different species. More comparison of the conductivities between this work and other perovskite Na-ion conductors (including RP phases). Porosity corrected relative permittivity calculation. See DOI: 10.1039/d1ta04252a

in mobile or large-scale systems such as electric vehicles and grid storage.[2] As a result, solid electrolytes serve as a good replacement for current liquid and polymer–gel electrolytes, owing to their high-temperature tolerance, longer lifetime, low toxicity, potential to enable higher energy density electrodes, and simple cell design.[3] For the reasons mentioned above, all-solid-state sodium ion batteries are promising for next-generation energy storage systems, especially for large-scale applications. Although significant developments have been made in solid electrolyte materials for sodium ion transport such as the discovery of β″-alumina and NASICONs, practical issues such as high mechanical stiffness, poor interface stability *vs.* high voltage electrodes, manufacturing challenges, and low room-temperature conductivity still limit their applications in full cells.[4–7] Alternative superionic conductors for solid electrolyte materials in sodium batteries are clearly needed, and moreover, the strategies and design principles for their development need to be established.

The double perovskite lithium-ion conductor system $Li_{3x}La_{2/3-x}TiO_3$ (LLTO) has been shown to exhibit high ionic conductivity and a relatively wide electrochemical window.[8,9] In addition, Ruddlesden–Popper (RP) layered perovskites consisting of ABO_3 perovskite slabs with alkali ion layers are also potential candidates for solid-state lithium-ion conductors.[10] While sodium ion conduction has been investigated between the interlayer planes of RP layered perovskites,[11–13] sodium ion transport within ABO_3 perovskite slabs in LLTO-type perovskites has not yet been widely studied.[14,15] This omission is despite the fact that, in general, ion transport within a perovskite is likely more 3-dimensional compared to that in RP-phase interlayers, particularly if the perovskite is disordered.

In this study, we aimed to synthesize a new class of sodium ion conductors based on the LLTO-type perovskite structure. Previous studies by Rivera *et al.*[14] and Ruiz *et al.*[15] suggested that Na^+ conductivity is low in an unsubstituted (*i.e.*, La and Ti remain) or unexpanded LLTO structure. Because of the larger ionic radius of sodium compared to lithium, we hypothesized that larger conduction channels are needed. The lattice can be expanded for sodium ion conduction by the substitution of B- and A-site framework cations with larger Zr^{4+} and Ba^{2+}, respectively. With these substitutions, sodium lanthanum zirconate (NLZ) and sodium lanthanum barium zirconate (NLBZ) were synthesized with similar but expanded structures to LLTO perovskites for sodium ion conduction. Seeking to improve the level of sodium ion conductivity, we varied the synthesis temperature, initial composition, and Nb dopant concentration, to manipulate the relative density and defect chemistry, particularly the sodium sub-stoichiometry. The resulting microstructures, phase compositions, and chemical compositions were analyzed in order to provide insights into the structure–property relationships. Conductivities of NLZ and NLBZ were compared to investigate the effect of different defect chemistries and lattice parameters. DC and AC electrical properties were also systematically measured in various conditions (*i.e.*, *vs.* oxygen partial pressure, humidity, temperature, and with different electrodes) to identify charge carriers, determine transference numbers, and observe the interactions between various possible carrier species (*e.g.*, sodium ions, electrons, holes, oxygen ions, protons). To better understand the results, density functional theory simulations were performed to evaluate the stability of the new phases as a function of composition. We find that these materials exhibit predominantly sodium ion conduction in dry, relatively oxidizing conditions; they are therefore new sodium-ion-conducting solid electrolytes. The Na-ion conductivities of the enlarged NLZ and NBLZ exceed that of the unexpanded $Na_{0.42}La_{0.525}TiO_3$ lattice by factors of ~19 (conventional sintering)/~49 (spark plasma sintering) and ~7, respectively, and the conductivity of NLZ reaches a value similar to that of $NaNbO_3$, despite the lower carrier concentration. We also conclude that ultimately, conductivity in bulk samples is limited by kinetic challenges with densification and thermodynamic bounds on the sodium ion deficiency that can be achieved in the perovskite phase. Based on these results, we suggest that non-equilibrium synthesis routes to form metastable defect configurations within more dense structures may be the best strategy forward for this class of Na-ion conductors, in future work.

2 Methods

2.1 Pellets fabrication

Sodium Lanthanum Zirconate (NLZ) (formula: $Na_xLa_{2/3-1/3x}ZrO_3$, abbreviated as NLZ–N*x*), Sodium Lanthanum Barium Zirconate (NLBZ) (formula: $Na_xLa_{1/3-1/3x}Ba_{0.5}ZrO_3$, abbreviated as NLBZ–N*x*), and Sodium Lanthanum Niobium Zirconate (formula: $Na_xLa_{2/3-1/3x}Zr_{1-y}Nb_yO_3$, abbreviated as NLBZ-N*x*-Nb*y*) nano-powders were synthesized by a modified Pechini method. Stoichiometric amounts of the starting reactants were dissolved in deionized water in a beaker, except that an extra 10% of $Na(NO_3)$ was added to compensate for Na loss during heat treatments in all compositions. Solutions were stirred for 30 minutes at 80 °C, followed by the addition of citric acid with stirring for 30 more minutes at 80 °C to allow chelation, followed by addition of ethylene glycol for polyesterification, with stirring at 80 °C until the solution became a gel. The molar ratios of metal cations : citric acid : ethylene glycol were 1 : 3 : 9 for all samples. After the polyesterification, the resin was dried at 240 °C for 10 hours (h). The dried gel was then crushed and calcined at 800 °C in air for 4 h. The NLZ and NLBZ pellets were fabricated by pressing the as-calcined powders uniaxially under 125 MPa with a hydraulic press (Carver, Model 4350). The compact green bodies were then sintered in a box furnace in air for various temperature and time combinations, as discussed in the Results section. A tetragonal yttria stabilized zirconia (formula: $(ZrO_2)_{0.97}(Y_2O_3)_{0.03}$, abbreviated as YSZ) pellet, used in transference number studies, was synthesized by pressing as-purchased YSZ powders (Sigma Aldrich, 99.99%) uniaxially under 125 MPa and sintering at 1200 °C in air for 6 h in a box furnace (YSZ-(1200C 6hr)). All sintering steps were carried out in sacrificial powders of the same compositions to minimize cation volatilization. Chemicals used include $Na(NO_3)$ (sodium(I) nitrate anhydrous, Fisher Chemicals, 99%), $La(NO_3)_3\cdot 6H_2O$ (lanthanum(III) nitrate hydrate, Sigma-Aldrich, 99.99%), $Ba(NO_3)_2$ (barium(II) nitrate anhydrous, Fisher

Chemicals, 99.99%), $ZrO(NO_3)_2 \cdot xH_2O$ (zirconium(IV) oxynitrate hydrate, Sigma-Aldrich, 99%), $(NH_4)NbO(C_2O_4)_2 \cdot xH_2O$ (ammonium niobate(V) oxalate hydrate, Sigma-Aldrich, 99.99%), $C_6H_8O_7$ (citric acid anhydrous, Fisher Chemicals, 99.5%), $(CH_2OH)_2$ (ethylene glycol, Fisher chemicals), and $(ZrO_2)_{0.97}(Y_2O_3)_{0.03}$ powders (zirconium(IV) oxide-yttria stabilized, Sigma-Aldrich, 99.99%). Water contents of starting reagents were measured by separate mass-loss analysis.

2.2 Characterization

The densities of the samples were determined from measured masses and geometries of the pellets, and expressed in terms of their respective theoretical densities (measured density/theoretical density = %TD). The phases of NLZ and NLBZ pellets were examined by X-ray powder diffraction (XRD) (Bruker D8 Advance XRD, Cu Kα-radiation, step size: 0.01°, time per step: 0.1 second, Panoramic Soller Slit) unless otherwise specified. High-resolution synchrotron powder diffraction data were collected using the rapid access program of beamline 11-BM at the Advanced Photon Source (APS), Argonne National Laboratory with a wavelength of 0.458 Å on selected samples (step size: 0.001°, time per step: 1 second). Rietveld refinements to all X-ray powder diffraction data were performed using TOPAS with Powder Diffraction Files (PDF) from International Centre for Diffraction Data (ICDD) database[16] for phase quantification and lattice parameter refinement.

The microstructure and grain size of pellets were characterized by scanning electron microscopy (JEOL 7000F Analytical SEM). For the electrical measurements, samples were coated on both faces with electrodes, and Pt wires were attached as current collectors. Au electrodes deposited by sputtering are very commonly used for cation conductors and were applied for all the measurements unless otherwise specified. A systematic experimental comparison and discussion of the effect of electrode metal choice (Au, Ag, Pt) is given in the ESI (Sec. 2†). Two-point AC impedance spectroscopy measurements (Ametek/Solartron ModulabXM ECS impedance analyzer with femtoammeter and potentiostat attachments) were carried out from 300 °C to 600 °C in Ar/O_2 mixtures over a range of oxygen partial pressures under dry or humid conditions. A water vapor pressure of 0.0121 atm was used in humid conditions by passing gas mixtures through a bubbler containing deionized water at 10 °C. All ionic conductivity measurements were carried out over a frequency range of 1 MHz to 100 mHz unless otherwise specified. The impedance spectra were analyzed by equivalent circuit fitting with a (RQ) circuit (Boukamp notation) or observing the low-frequency real axis intercept to determine the total resistance. A geometric correction according to the dimensions of the pellets was done to calculate measured conductivity from the measured resistance. A porosity correction was also performed based on Bruggeman symmetric medium theory, assuming pores to be completely insulating.[17–19] Impedance spectra were analyzed with a "Distribution of Relaxation Times" (DRT) approach, using DRTtools software.[20] DC polarization experiments were performed using porous sputtered Au electrodes and a constant applied voltage of 0.3 V, with monitoring of the current as a function of time. Additional measurements and DRT analysis of the effect of different electrodes (Ag, Pt) can be seen in Sec. 2 in ESI.†

The following abbreviations were used:

- NLZ-Nx powders: as calcined powders with cation ratio of Na : La : Zr = x : 2/3 − 1/3x : 1 ($0 < x < 0.5$).
- NLZ-Nx-(temperature time): NLZ-Nx powders pressed uniaxially under 125 MPa and sintered at a certain temperature. For example, NLZ-N0.5-(1200C 6hr) is sintered under 1200 °C for 6 hours.
- NLZ-Nx-Nby powders: as calcined powders with cation ratio of Na : La : Zr : Nb = x : 2/3 − 1/3x : 1 − y : y ($0 < x < 0.5$) ($0 < y < 1$).
- NLZ-Nx-Nby-(temperature time): NLZ-Nx-Nby powders pressed uniaxially under 125 MPa and sintered at a certain temperature. For example, NLZ-N0.5-Nb0.05-(1200C 6hr) is sintered under 1200 °C for 6 hours.
- NLBZ-Nx powders: as calcined powders with cation ratio of Na : La : Ba : Zr = x: 1/3 − 1/3x : 0.5 : 1 ($0 < x < 0.25$).
- NLBZ-Nx-(temperature time): NLBZ-Nx powders pressed uniaxially under 125 MPa and sintered at a certain temperature. For example, NLBZ-N0.25-(1200C 6hr) is sintered under 1200 °C for 6 hours.

2.3 Computation

Density functional theory[21,22] calculations were performed using the Vienna *Ab Initio* Software Package (VASP).[23,24] The Projector Augmented Wave (PAW) method was used to model the core electrons in the crystal. The Perdew–Burke–Ernzerhof (PBE) generalized gradient approximation (GGA) to the exchange–correlation functional was employed. The orbitals were expanded in a plane wave basis set with an energy cutoff of 520 eV. For every compound that was simulated, geometry optimization was carried out until the forces on each atom were reduced below 10^{-4} eV Å^{-1}. DFT-computed energies of both the compounds under consideration as well as competing binaries, ternaries, and elemental phases were used to create chemical potential and composition space phase diagrams.

3 Results

3.1 Structural characterization

3.1.1 NLZ-Nx with different heat treatment and starting stoichiometry. As described, all NLZ-Nx powders were synthesized by a modified Pechini method with a calcining step of 800 °C for 4 h to keep the size of the particles small as well as preventing Na loss.[25] The XRD patterns of NLZ-Nx powders and sintered pellets of different heat treatments and initial stoichiometry are shown in Fig. 1, and a summary of their phase fractions and densities can be seen in Table 1. It should also be noted that a trace amount of an unidentified impurity phase was present in all sintered NLZ samples, and the peak positions and broad width may be consistent with adventitious nanocrystalline carbonate-hydroxide surface phase, given air exposure during XRD measurement. Due to the very minor peak intensity, it is unlikely to have a significant effect on our

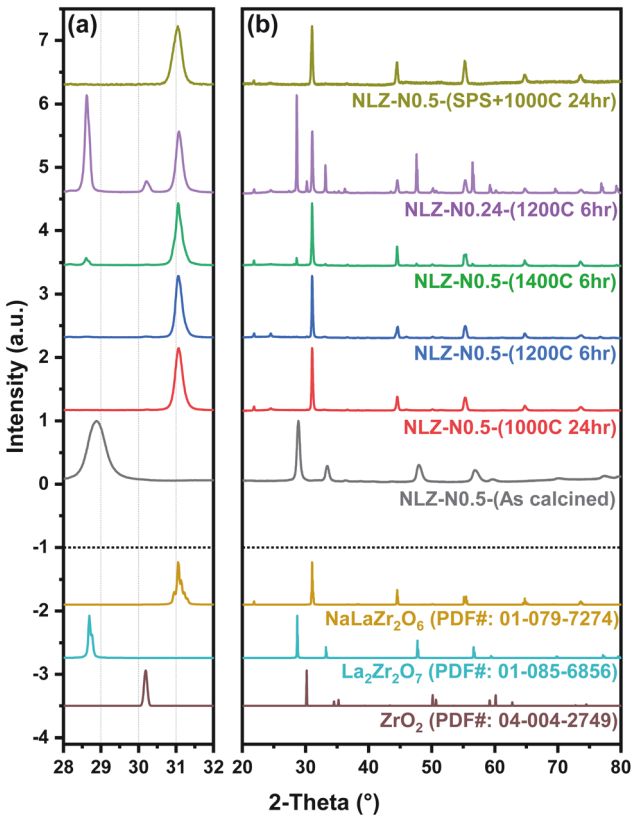

Fig. 1 Experimental X-ray diffraction profiles for NLZ-N*x* with different heat treatments and initial stoichiometries, and calculated XRD profiles from ICDD[16] for the observed phases. The higher resolution data in the range of 2-theta = 28°–32° includes the most intense reflections for the perovskite, pyrochlore and zirconia phases.

analysis. The as-calcined powders were in a distorted $La_2Zr_2O_7$-like pyrochlore phase before sintering. After sintering, a nominally pure $Na_{0.5}La_{0.5}ZrO_3$ perovskite phase was observed for sintering conditions of 1000 °C for 24 h and 1200 °C for 6 h, with similar densities. The nominal stoichiometry given to the $Na_{0.5}La_{0.5}ZrO_3$ perovskite phase (and all other reported perovskite phases) is presumed based on the targeted compositions and is used as a label to facilitate consistent distinction between observed phases in XRD analysis. Chemical analysis by inductively coupled plasma (ICP) also showed agreement with the nominal composition, within uncertainty (as determined by replicate analysis). The average grain size increased from 252 nm to 375 nm when sintering temperature was increased from 1000 °C to 1200 °C, as seen in Fig. 2(a) and (b). Sintering at 1400 °C for 6 h resulted in higher density with a minor $La_2Zr_2O_7$ pyrochlore-like secondary phase. ICP also confirmed Na deficiency after this higher temperature (1400 °C) sintering. To achieve higher density, spark plasma sintering (SPS) was performed on NLZ-N0.5 powders at 700 °C and 500 MPa for 3 minutes, with a post-annealing step using conventional sintering at 1000 °C for 24 h (abbreviated as NLZ-N0.5-(SPS+1000C 24hr)). XRD showed a nominally pure $Na_{0.5}La_{0.5}ZrO_3$ perovskite phase, and a higher density of 73 ± 5%. However, the SPS treated sample was fragile and cracked into several small pieces, inevitably leading to some degree of uncertainty in the geometry evaluation process. As a result, an error bar was included to indicate the level of uncertainty for the density measurements. The microstructure of NLZ-N0.5-(SPS+1000C 24hr) also appeared to be denser, with comparable grain size to NLZ-N0.5-(1000C 24hrr), as seen in Fig. 2(d).

Intentionally Na-deficient NLZ-N0.24 powders were also synthesized using the same procedure with different starting stoichiometry. After sintering under 1200 °C for 6 h, large amounts of $La_2Zr_2O_7$ pyrochlore-like phase and t-ZrO_2-like phase were formed. For all these samples with different sintering conditions and different starting stoichiometries, different amounts of impurity phases were formed; however, the peak position of the $Na_{0.5}La_{0.5}ZrO_3$ perovskite phase remained unchanged. NLZ-N0.5 doped with 5% of Nb was also prepared following the same synthesis procedure, with a stoichiometry of Na : La : Zr : Nb = 0.5 : 0.5 : 0.95 : 0.05 (NLZ-N0.5-Nb0.05). After sintering under 1200 °C for 6 h, 11.9 wt% of $La_2Zr_2O_7$ pyrochlore-like phase was formed. The peak positions of the Nb-doped perovskite phase were also shifted to higher angles relative to the NLZ peaks as seen in Fig. 3. Phase fractions and densities of NLZ-N*x* and NLZ-N*x*-Nb*y* are summarized in Table 1 according to different heat treatment and starting stoichiometries.

3.1.2 NLBZ-N*x* with different heat treatment and starting stoichiometry. NLBZ-N*x* powders were synthesized using the same procedure as NLZ-N*x*. The XRD data for the NLBZ-N*x* powders and sintered pellets after different heat treatment, as well as different starting Na stoichiometries, are shown in Fig. 4. The densities and phase fractions are further summarized in Table 2.

Table 1 Phase fractions and densities of NLZ-N*x* and NLZ-N*x*-Nb*y* with different heat treatments and initial stoichiometries. R_{wp} values from Rietveld refinements are also listed here. (Tetragonal fluorite ZrO_2-like phase is abbreviated as t-ZrO_2. An unidentified trace impurity phase was also detected in NLZ samples in XRD, but not included in refinement or listed in the table; see text.)

	Perovskite (wt%)	Pyrochlore (wt%)	t-ZrO_2 (wt%)	Density (%TD)	R_{wp} (%)
NLZ-N0.5-(1000C 24hr)	100	0.0	0.0	46.4	7.83
NLZ-N0.5-(1200C 6hr)	100	0.0	0.0	47.1	13.40
NLZ-N0.5-(1400C 6hr)	94.6	5.4	0.0	60.5	9.93
NLZ-N0.5-(SPS+1000C 24hr)	100	0.0	0.0	73 ± 5	7.96
NLZ-N0.24-(1200C 6hr)	46.1	45.9	8.0	—	11.20
NLZ-N0.5-Nb0.05-(1200C 6hr)	88.1	11.9	0.0	—	11.97

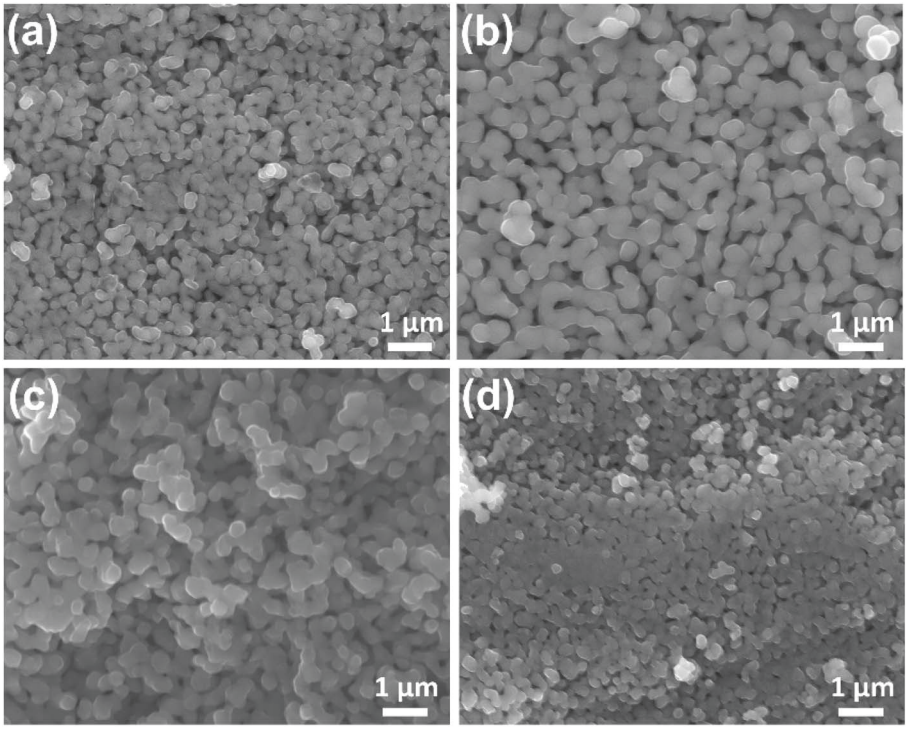

Fig. 2 SEM images of (a) NLZ-N0.5-(1000C 24hr), (b) NLZ-N0.5-(1200C 6hr), (c) NLBZ-N0.25-(1200C 6hr) and (d) NLZ-N0.5-(SPS+1000C 24hr).

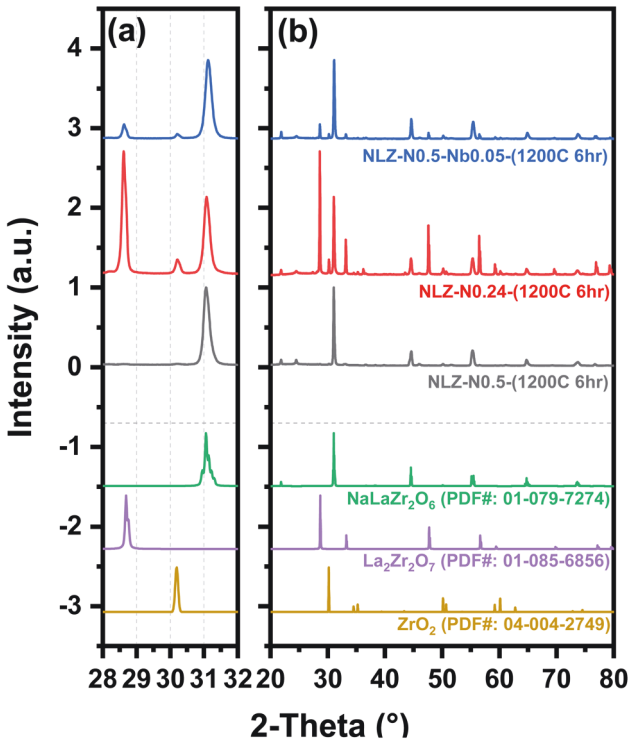

Fig. 3 Experimental X-ray diffraction profiles for NLZ with different levels of doping, and calculated XRD profiles from ICDD[16] for the observed phases. The higher resolution data in the range of 2-theta = 28°–32° includes the most intense reflections for the perovskite, pyrochlore and zirconia phases.

For the as-calcined NLBZ-N0.25 powders, XRD revealed a mixture of two perovskite phases, which could be fitted to structures closely resembling $BaZrO_3$ and $Na_{0.5}La_{0.5}ZrO_3$. After sintering at 1000 °C for 24 h, the peaks of $BaZrO_3$ phase shifted to higher angles (lattice contracted), whereas the peaks of $Na_{0.5}La_{0.5}ZrO_3$ shifted towards lower angles (lattice expanded), but both perovskite phases were retained. Further heat treatment of 1000 °C for 48 h resulted in very little changes in the peak positions either perovskite phase, while a slight increase in the amount of the $La_2Zr_2O_7$-like pyrochlore phase was observed. Sintering at 1200 °C for 6 h gave rise to a single perovskite phase with the nominal composition $Na_{0.25}La_{0.25}Ba_{0.5}ZrO_3$ and density similar to NLZ-N0.5-(1200C 6hr). Minor formation of the $La_2Zr_2O_7$ pyrochlore-like phase was observed. The average grain size was measured to be 383 nm, as seen in Fig. 2(c). Sintering at 1400 °C for 6 h resulted in a shift in the NLBZ perovskite peaks to lower angles and an increase of $La_2Zr_2O_7$ pyrochlore-like phase fraction. The density also increased, consistent with NLZ-N0.5-(1400C 6hr). As was the case for the NLZ compositions, samples of lower Na content in the starting powders were also synthesized. XRD showed that NLBZ-N0.125-(1200C 6hr) was composed of a NLBZ perovskite phase with the same peak positions as NLBZ-N0.25-(1400C 6hr) and 15.4 wt% $La_2Zr_2O_7$ pyrochlore-like phase.

3.2 Electrical measurements

Measured conductivity (σ_m) is calculated according to pellet geometry ($\sigma_m = R \times A/L$, where R is the resistance, A is the electrode area, and L is the sample thickness). The low density

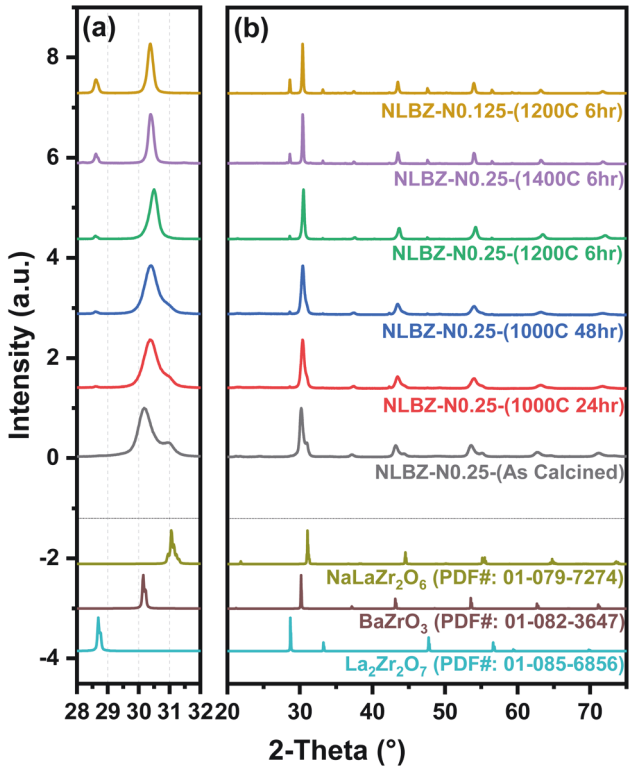

Fig. 4 Experimental X-ray diffraction profiles for NLBZ-N*x* with different heat treatments and initial stoichiometries, and calculated XRD profiles from ICDD[16] for the observed phases. The higher resolution data in the range of 2-theta = 28°–32° includes the most intense reflections for the perovskite, pyrochlore and zirconia phases.

of the sintered pellets required that the measured conductivity data be corrected using the Bruggeman symmetric medium theory,[17–19] where both high conductivity and low conductivity phases are assumed to be isotropic and non-wetting to each other. In the case of porous samples, the high conductivity phase is the material itself, whereas the low conductivity phase is the pore space, assumed to be completely insulating. As a result, the porosity correction can be described by eqn (1):

$$\sigma_m = \sigma_h\left[1 - \frac{3}{2}f\right] \quad (1)$$

Table 2 Phase fractions and densities of NLBZ-N*x* with different heat treatments and initial stoichiometries. R_{wp} values from Rietveld refinements are also listed here

	Perovskite (wt%)	Pyrochlore (wt%)	Density (%TD)	R_{wp} (%)
NLBZ-N0.25-(1200C 6hr)	98.0	2.0	44.5	9.23
NLBZ-N0.25-(1400C 6hr)	90.6	9.4	59.4	11.79
NLBZ-N0.125-(1200C 6hr)	84.6	15.4	45.4	10.89

σ_m is the measured conductivity, σ_h is the porosity corrected conductivity, representing the conductivity of the material matrix, and f is the volume fraction of the porosity.[18,26] Impurity phases are also included and considered to be completely insulating.

Assuming a hopping mechanism, which most ionic conductors follow, the temperature-dependent conductivity can be described by the Arrhenius equation, and the activation energy can be calculated from the data by fitting with eqn (2):

$$\sigma_h = \frac{\sigma_0}{T}\exp\left(\frac{-E_A}{k_B T}\right) \quad (2)$$

Here, σ_0 is the conductivity pre-factor, T is the temperature during measurements, E_A is the activation energy for ion hopping, and k_B is the Boltzmann constant.

3.2.1 Electrical properties of NLZ-N0.5-(1200C 6hr) and NLZ-N0.5-(SPS+1000C 24hr). Electrical measurements for NLZ-N0.5-(1200C 6hr) were performed with porous Au electrodes unless otherwise specified. Fig. 5(a) shows a typical Nyquist plot of NLZ-N0.5-(1200C 6hr) pellet with sputtered Au electrodes on both faces. The semicircle at high frequencies can be attributed to the sample response, whereas the feature at low frequencies is attributed to the electrode response. These attributions are made based on (a) the relative permittivity of the high frequency feature obtained from the porosity-corrected capacitance (see ESI Sec. 5†) and (b) the influence of electrode metal choice on the low frequency response (see ESI Sec. 2†). The high-frequency response attributed to the sample was first analyzed with a DRT approach, using DRTtools program;[20] the results suggest only one relaxation time with Au electrodes (Fig. S5†). Thus, the high-frequency arcs of the impedance spectra were analyzed with an (RQ) equivalent circuit in order to determine the total sample resistance, and the uncertainty in fitting was estimated to be within 5–10%. The porosity-corrected relative permittivities (ε_r) of the sample response were between 294 and 252 in dry environments (300–600 °C) for NLZ-N0.5-(1200C 6hr), which are comparable to those of similar perovskite compositions.[27,28]

Measurements were performed under different pO_2 and different humidity at various temperatures to determine whether electronic species (holes, electrons) and/or protons contribute to total conductivities. The total conductivity in dry environments followed the Arrhenius equation very well, and the results were almost identical when measured under different pO_2s ranging from 10^{-5} to 1 atm, as seen in Fig. 6(a). At $pO_2 = 10^{-5}$ atm, the activation energy is calculated to be 0.80 eV; at $pO_2 = 1$ atm, the activation energy is calculated to be 0.81 eV; within error, these are the same. The porosity-corrected total conductivity of NLZ-N0.5-(1200C 6hr) is 4.25×10^{-7} S cm^{-1} at 300 °C. In humid environments, on the other hand, the conductivity was very similar with the results from dry environments only in the high temperature range (400–600 °C), whereas a decrease in conductivity was observed under humid conditions in the low temperature range (300–400 °C).

When total conductivity is measured by AC impedance spectroscopy, all mobile charge carriers can contribute to the total conductivity. In dry environments measured with Au electrodes, four possible species could have contributed to the

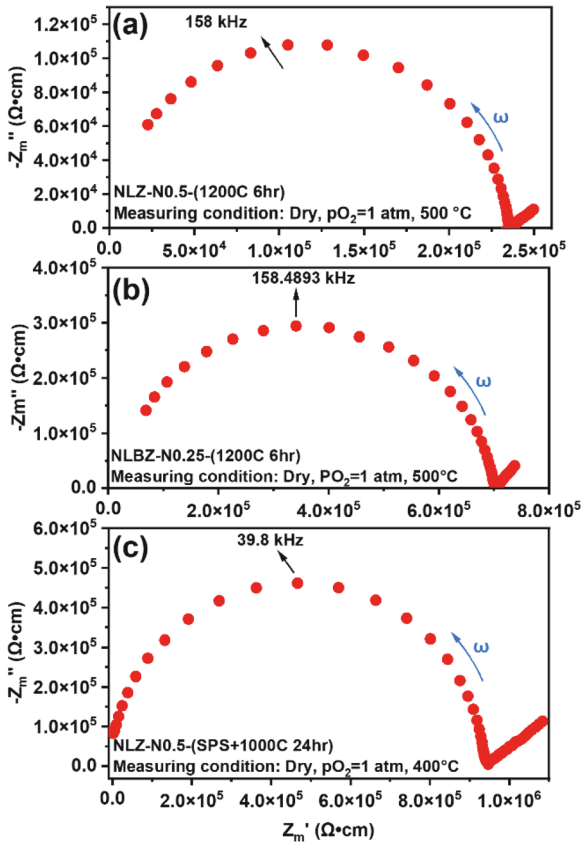

Fig. 5 Typical Nyquist plots of (a) NLZ-N0.5-(1200C 6hr), (b) NLBZ-N0.25-(1200C 6hr), (c) NLZ-N0.5-(SPS+1000C 24hr), measured in dry, $pO_2 = 1$ atm gas environment at 500 °C. Z_m' and Z_m'' are respectively the real and imaginary part of the impedance that is geometry corrected and not porosity corrected.

total conductivity: sodium ions, oxygen ions, holes, and electrons. Total conductivities for NLZ-N0.5-(1200C 6hr) were independent of pO_2 indicating that electronic defects (electrons, holes) likely do not contribute significantly to the measured total conductivity, *i.e.*, that transference number (t_{elec}) were negligible. In order to determine the transference numbers of sodium ions and oxygen ions, DC polarization experiments[29,30] were first performed on YSZ-(1200C 6hr) using a constant voltage of 0.3 V across the faces of the sample contacted with sputtered porous Au electrodes. The current response was measured over time, as seen in Fig. 7(c). With YSZ being a known oxygen-ion conductor, the current was almost invariant over time, as the porous electrodes are not blocking to oxygen. In order to quantify the transference number for oxygen conduction (t_O) of NLZ-N0.5-(1200C 6hr), the same DC polarization experiments were performed. The current response was measured over time, as seen in Fig. 7(a). This was done at 600 °C in the dry condition under $pO_2 = 1$ atm. The current density decreased and reached a plateau after 8×10^4 seconds, and $I_{final}/I_{initial}$ is calculated to be 0.0325. As sputtered Au electrodes are only blocking to sodium ions, the sodium ion transference number (t_{Na}) is calculated to be 0.9675. More detailed analysis of the transference numbers can be found in Sec. 3 of the ESI.†

Additionally, AC impedance spectroscopy was also performed on NLZ-N0.5-(SPS+1000C 24hr). Because of the fragile nature of the SPS sample (see Sec. 3.1.1), the handling of sample was kept to a minimum, using Ag paste as electrodes, and measured in the range of 300–400 °C in $pO_2 = 1$ atm. In the case of NLZ-N0.5-(SPS+1000C 24hr) measured using Ag electrodes, only one arc was observed in the impedance spectrum, as seen in Fig. 5(c). DRT analysis also showed that there was only one process in all the spectra (Fig. S5(h)†); more discussion concerning the feasibility of using Ag electrodes on this denser sample can be found in Sec. 2 in the ESI.† The porosity-corrected conductivities of NLZ-N0.5-(SPS+1000C 24hr) were higher than those of conventionally sintered NLZ-N0.5-(1200C 6hr), as seen in Fig. 8. The activation energy of NLZ-N0.5-(SPS+1000C 24hr) was calculated to be 0.81 eV, identical with that of NLZ-N0.5-(1200C 6hr). Error bars were also included due

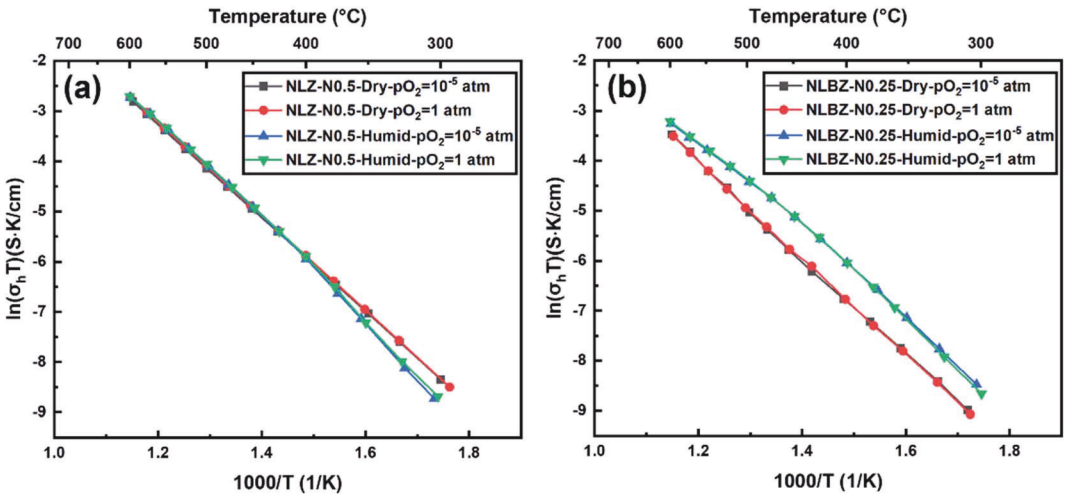

Fig. 6 Arrhenius plots of porosity corrected total conductivity (σ_h) of (a) NLZ-N0.5-(1200C 6hr), (b) NLBZ-N0.25-(1200C 6hr) in different gas environments and humidity.

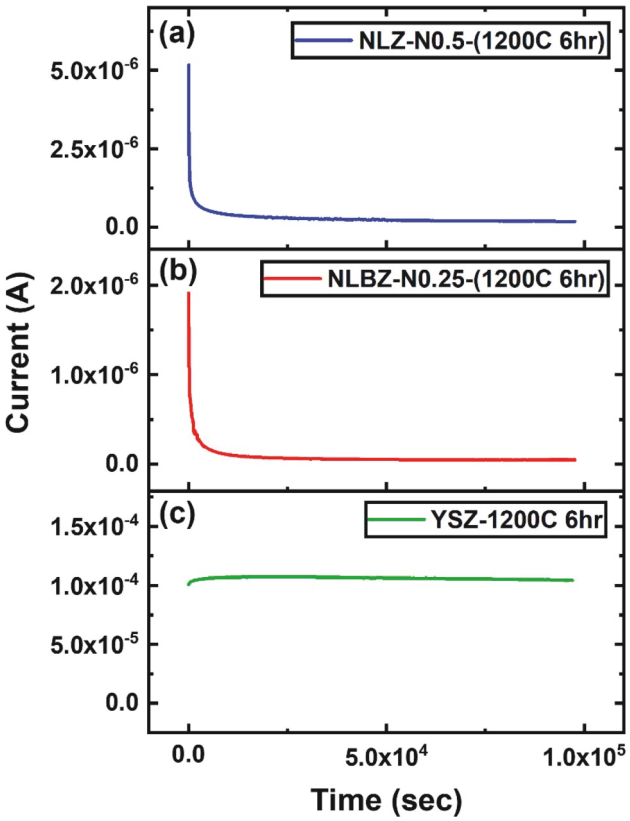

Fig. 7 Current response with respect to time under an applied voltage of 0.3 V for (a) NLZ-N0.5-(1200C 6hr) (b) NLBZ-N0.25-(1200C 6hr) (c) YSZ-(1200C 6hr) in dry, $pO_2 = 1$ atm gas environment at 600 °C.

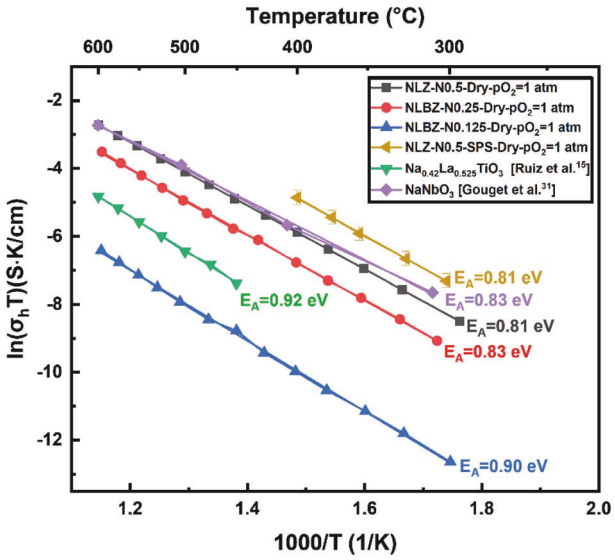

Fig. 8 Arrhenius plots of porosity corrected total conductivity (σ_h) of NLZ-N0.5-(1200C 6hr), NLBZ-N0.25-(1200C 6hr), NLBZ-N0.125-(1200C 6hr), and NLZ-N0.5-(SPS+1000C 24hr) in dry $pO_2 = 1$ atm environment. Total conductivities of $Na_{0.42}La_{0.525}TiO_3$ (Ruiz *et al.*[15]) and $NaNbO_3$ (Gouget *et al.*[31]) are also shown here for comparison. Note that 12% of the conductivity of $NaNbO_3$ shown here is contributed by O^{2-}.[31]

to the uncertainty in geometry/density evaluation because of the small sample size.

3.2.2 Electrical properties of NLBZ-N0.25-(1200C 6hr). Fig. 5(b) shows a typical impedance spectrum of NLBZ-N0.25-(1200C 6hr) with sputtered Au electrodes on both faces. Similar impedance spectra were observed for NLBZ-N0.25-(1200C 6hr) and the earlier NLZ-N0.5-(1200C 6hr); therefore, the same procedures for fitting and measurements were used. The relative permittivities (ε_r) of the sample response were between 1071 and 1411 in dry environments (300–600 °C) for NLBZ-N0.25-(1200C 6hr). The total conductivity in dry environments followed the Arrhenius equation well and the results were very similar when measured under different pO_2, from 10^{-5} atm to 1 atm. Electrical measurements in dry environments under $pO_2 = 10^{-5}$ atm and $pO_2 = 1$ atm were almost identical at all temperatures. At $pO_2 = 10^{-5}$ atm, the activation energy is calculated to be 0.83 eV; at $pO_2 = 1$ atm, the activation energy is calculated to be 0.83 eV, *i.e.*, the same within error. The porosity-corrected total conductivity of NLBZ-N0.25-(1200C 6hr) is 1.63×10^{-7} S cm^{-1} at 300 °C. In humid environments, the conductivity was increased for both $pO_2 = 10^{-5}$ atm and $pO_2 = 1$ atm across the whole temperature range (300–600 °C), relative to the dry environments, as seen in Fig. 6(b).

Similar to NLZ, the conductivities of NLBZ-N0.25-(1200C 6hr) are also not pO_2 dependent, indicating negligible t_{elec}. The same DC polarization experiments were performed with the current response measured as a function of time, as seen in Fig. 7(b). At 600 °C in dry, $pO_2 = 1$ atm environment, the current density reached a plateau after 8×10^4 seconds and $I_{final}/I_{initial}$ is calculated to be 0.0224. t_{Na} is calculated to be 0.9776. Additional discussion on transference numbers can be seen in Sec. 3 of the ESI.†

Electrical measurements were also performed on NLBZ-N0.125-(1200C 6hr) with sputtered Au electrodes in $pO_2 = 1$ atm and dry environments for comparison, to observe the effect of sodium deficiency. Recall from Table 2 that this sample contained a larger amount of the minor pyrochlore phase and a slight shift in perovskite phase XRD peaks relative to the NLBZ-N0.25-(1200C 6hr) sample. The pyrochlore phase was assumed to be completely insulating in the conductivity magnitude correction process. The total conductivity of the Na-deficient perovskite phase was significantly lower compared to both NLZ-N0.5-(1200C 6hr) and NLBZ-N0.25-(1200C 6hr), as seen in Fig. 8. Of note, both NLZ-N0.5-(1200C 6hr) and NLBZ-N0.25-(1200C 6hr) exhibited significantly higher conductivities and lower activation energies compared to non-expanded $Na_{0.42}La_{0.525}TiO_3$ (Ruiz *et al.*[15]), *i.e.*, the case where Na simply substitutes for Li in LLTO. At 300 °C, the conductivities were ~19× and ~7× higher for NLZ-N0.5-(1200C 6hr) and NLBZ-N0.25-(1200C 6hr), respectively. The conductivity of NLZ-N0.5-(1200C 6hr) was also comparable with that of $NaNbO_3$ (Gouget *et al.*[31]), which suffers from non-negligible oxygen ion conductivity. Promisingly, although mechanically less robust, NLZ-N0.5-(SPS+1000C 24hr) was ~49× more conductive than

$Na_{0.42}La_{0.525}TiO_3$ (ref. 15) at 300 °C. An in-depth discussion of these trends and magnitudes can be found in Sec. 4.3.3.

4 Discussion and supporting simulations

4.1 Limits to thermodynamic stability and defect engineering of NLZ-N*x*

One pillar of our strategy for producing Na-ion conducting perovskites was defect engineering, *i.e.*, the intentional generation of Na vacancies (v'_{Na}). This route was pursued because it is known that in the LLTO analogous structure, Li ions move by an A-site vacancy mechanism.[8,9,32,33] To a first approximation, an increased Na-vacancy concentration is therefore expected to raise the ionic conductivity pre-exponential factor (σ_0) by increasing the availability of adjacent vacant sites for any given Na-ion to hop to. For isolated ion hopping in a non-concerted mechanism, σ_h can be expressed as:

$$\sigma_h = \frac{\gamma(Nc)Z(1-c)a^2(z_i e)^2\nu_0}{k_B T}\exp\left(\frac{\Delta S_m}{k_B}\right)\exp\left(\frac{-\Delta H_m}{k_B T}\right) = \frac{\sigma_0}{T}\exp\left(\frac{-\Delta H_m}{k_B T}\right) \quad (3)$$

where γ is the geometric and correlation factor, N is the volumetric concentration of possible sites for the charge carrier, c is the site fraction of the charge carrier, Z is the coordination number of the charge carrier (number of nearest neighbor sites), a is the jump distance, $z_i e$ is the charge ($e = 1.6 \times 10^{-19}$ C) of the charge carrier i, ν_0 is the jump attempt frequency, ΔS_m is the migration entropy, and ΔH_m is the migration enthalpy.[34] By introducing Na vacancies to a limited extent, the $c(1-c)$ term is increased, raising the σ_0.

As noted previously, Na vacancies were pursued by three routes: (1) Na loss through long/hot sintering, (2) Na-deficient initial composition, and (3) Na vacancy generation through donor doping. The following sub-sections interpret the effectiveness of each of these approaches. We discuss the possible reasons for the phases and structures formed in the context of existing literature, the reasons for limits to Na vacancy formation in the perovskite phase with computational support, and the implications for transport. Synthesis of NLZ-N*x* was carried out with two different starting stoichiometries: NLZ-N0.5 and NLZ-N0.24, along with different sintering conditions or Nb-doping for NLZ-N0.5. Prior to this work the $Na_{0.5}La_{0.5}ZrO_3$ phase had been synthesized for structural characterization and confirmed to be double perovskite,[35–37] but no electrical characterization was performed.

4.1.1 NLZ-N0.5: controlling Na deficiency by sintering temperature and time. Longer/hotter sintering can result in overall Na deficient compositions, relative to the initial composition, given the reasonably high vapor pressure of Na_2O.[25,38] To maintain electroneutrality, the v'_{Na} caused by loss of Na to the gas phase could be compensated ionically (*e.g.*, by $v^{\cdot\cdot}_O$) or electronically (*e.g.*, by $h^{\cdot}$). As an example of the former case, a partial Schottky reaction might take place with loss of both Na and O at high temperatures:

$$2Na^{\times}_{Na} + O^{\times}_{O} \rightarrow Na_2O(g) + 2v'_{Na} + v^{\cdot\cdot}_{O} \quad (4)$$

If this reaction dominates, the simplified electroneutrality condition (ENC) would be $[v'_{Na}] \approx 2[v^{\cdot\cdot}_O]$. For the second option of electronic compensation, again if dominant, the simplified ENC would be $[v'_{Na}] \approx h^{\cdot}$. For both of these cases, one might expect additional ionic/electronic charge carriers to contribute to the overall measured conductivity; however, the selectively blocking electrode DC polarization measurements (Sec. 3.2.1) demonstrated that conductivity was ~96% from Na ions. This result suggests that these reactions have not taken place to any significant degree, or are not dominant, or that charge-compensating defects are very deeply trapped. (In principle, Zr interstitial or anti-site defects could also charge-compensate for v'_{Na} formed by volatilization $[v'_{Na}] \approx 4[Zr^{\cdot\cdot\cdot\cdot}_i]$ or $[v'_{Na}] \approx 3[Zr^{\cdot\cdot\cdot}_{Na}]$, but these defects are likely energetically unfavorable.)

When the desired perovskite phase is unstable at the composition of the overall Na deficiency, secondary phases can form. During high temperature Na loss, the excess La and Zr in the structure can leave the perovskite to form separate oxide phases, for example:

$$Na_{0.5}La_{0.5}ZrO_3 \rightarrow Na_{0.5-x}La_{0.5-x}Zr_{1-2x}O_{3-6x} + \frac{x}{2}Na_2O(g) + La_xZr_xO_{3.5x} + xZrO_2 \quad (5)$$

(In this example, the perovskite is assumed to be a line compound that maintains its initial stoichiometry, but in practice the composition will be pinned at the Na-deficient boundary of the thermodynamic stability.) Other phases may also be observed in the context of kinetic limitations to perovskite phase formation during initial synthesis stages.

In the NLZ-N0.5 starting stoichiometry, XRD showed that the as-calcined powders were in a pyrochlore ($La_2Zr_2O_7$-like) phase, but after pressing and sintering, the powders were transformed into a $Na_{0.5}La_{0.5}ZrO_3$ perovskite phase. Since the NLZ-N0.5 powders were calcined at lower temperatures, and the $Na_{0.5}La_{0.5}ZrO_3$ perovskite phase was formed after sintering, it is not likely that the pyrochlore phase for the as-calcined powders was formed due to Na loss, when only minimal Na evaporation is expected at 800 °C.[25] Rather, this result indicates that the as-calcined NLZ-N0.5 powders were in a metastable pyrochlore phase. A change in peak positions relative to pure $La_2Zr_2O_7$ was also observed, suggesting that the pyrochlore phase was distorted *vs.* $La_2Zr_2O_7$, most likely due to a large amount of Na in the structure. After sintering above 1000 °C, a pyrochlore–perovskite phase transformation occurred, resulting in a stable $Na_{0.5}La_{0.5}ZrO_3$ perovskite phase. A further annealing step at 800 °C for 10 h did not result in any change in the phase fraction, confirming that the $Na_{0.5}La_{0.5}ZrO_3$ perovskite phase is stable after sintering. Similar behavior with a pyrochlore–perovskite phase transformation has been reported in (Pb,La)(Zr,Sn,Ti)O_3 systems, where a metastable pyrochlore phase is first formed from an amorphous phase at lower temperatures, and further heat treatment at higher temperature results in the formation of a perovskite phase.[39]

Our results at different sintering temperatures showed various amounts of the $La_2Zr_2O_7$-like pyrochlore impurity phase present. At 1000 °C for 24 h or 1200 °C for 6 h, the sintered pellet remained phase pure with densities of 46.4% and 47.1%, respectively. The low densities can be attributed to the poor sinterability of perovskite zirconate, as has been reported in some barium zirconate systems. A sintering temperature of 1600 °C and the addition of dopants for solid-state reactive sintering are usually needed to form dense samples of barium zirconate.[40,41] Higher temperature sintering was thus performed at 1400 °C for 6 h on pressed NLZ-N0.5 powders in order to increase the density of the pellet. The density was increased to 60.8%; however, 5.4 wt% of pyrochlore phase was formed due to Na loss under high sintering temperature. The formation of a pyrochlore phase has also been reported in $Li_7La_3Zr_2O_{12}$ (LLZO) garnet-type Li conductor due to a Li loss under heat treatments at higher temperatures.[42,43] A longer heat treatment for 96 h at a lower temperature of 1000 °C was also performed in an attempt to increase the density without significant Na loss. However, there was little increase in grain size from an average of 252 nm to an average of 280 nm between sintering for 24 h and 96 h at 1000 °C, no measurable change in density was observed, and a slight amount of $La_2Zr_2O_7$-like pyrochlore phase was formed. In these longer/hotter sintering conditions with Na loss, the resulting pyrochlore phase appears more likely to be thermodynamically stable unlike the peak-shifted metastable phase achieved following calcination of the precursor at lower temperatures. In addition to conventional sintering, a higher density of 73 ± 5% was achieved using SPS followed by a post-annealing step, without $La_2Zr_2O_7$-like pyrochlore phase formation. However, the SPS treated sample suffered from residual stress, making the sample fragile and prone to crack. Fortunately, a small piece of sample was still robust enough for electrical measurements. Furthermore, flash sintering was attempted under an electric field of 20 V mm^{-1} and a ramp rate of 20 °C min^{-1} in a dog bone geometry, with an identical setup demonstrated by Murray *et al.*,[44] but the sample did not flash up to 950 °C. A higher electric field of 40 V mm^{-1} was also attempted on a rectangular-shaped sample with Pt wires wrapped on the ends of the sample; however, a bright light and popping noise occurred, and the wires on the positive electrode had broken. These attempts resulted in inhomogeneous samples with large amounts of impurity phases.

In LLTO, Li stoichiometry can be tuned in a relatively wide range through changing the Li : La and thereby A : B-site ratios while maintaining the perovskite phase. Li deficiency has, to some degree, been shown to yield a lower activation energy for ionic conduction. This effect can be attributed to an increase of the lattice parameters due to the considerably larger lanthanum (1.032 Å) ion radius compared to that of the lithium ion (0.76 Å);[9,45] here, Li deficiency is accommodated by excess La. In addition, the introduction of Li vacancies (v'_{Li}) also affects the conductivity by modifying the charge carrier concentration (if considered to be vacancies) or available sites for hopping of carriers (if considered to be Li ions).[9,45,46] Despite the structural similarity to LLTO, the Na loss arising from higher temperatures or longer sintering times for the NLZ-N0.5 starting stoichiometry instead resulted in the formation of the pyrochlore impurity phase. The XRD peak positions of the NLZ perovskite phase were also examined for different sintering conditions. Our results showed that there is no change in peak positions of the NLZ perovskite phase, regardless of the amount of Na loss. It is possible that this invariability in peak position stemmed from very limited Na stoichiometry change in the NLZ perovskite phase; in other words, the perovskite structure may not be stable under Na deficient stoichiometry and thus allows very little v'_{Na} formation. It appears that dense and phase pure $Na_{0.5}La_{0.5}ZrO_3$ has not been synthesized before, most likely due to these reasons. The low density and likely low v'_{Na} concentration can explain some limitations to the ionic conductivity.

4.1.2 NLZ-N0.24: generating Na deficiency by starting composition. As a second approach, NLZ-N0.24 with a Na-deficient starting stoichiometry was synthesized in an effort to achieve a Na-deficient NLZ perovskite phase, thereby potentially increasing the conductivity through the introduction of v'_{Na}. In this case, considering the NLZ-N0.5 as a reference state, the v'_{Na} are charge-compensated by extrinsic addition of excess La on Na sites by design through maintenance of the $x : 2/3 - 1/3x$ ratio of Na : La in the synthesized composition. When this compensation mechanism is dominant, the simplified ENC may be considered $[v'_{Na}] \approx 2[La^{\cdot\cdot}_{Na}]$, with no generation of other ionic/electronic carriers required. Again, the low oxide ion and electronic transference numbers measured (Sec. 3.2.1) suggest that even other intrinsic/extrinsic defect reactions were also not significantly contributing these carriers.

Sintering the NLZ-N0.24 powders at 1200 °C for 6 h resulted in a significant amount of $La_2Zr_2O_7$-like pyrochlore phase and t-ZrO_2-like phase, as shown in Table 1, which is to be expected on account of the low Na content in the starting powders. Peak positions of the NLZ perovskite phase in NLZ-N0.24 were examined carefully, and no deviations from the NLZ-N0.5 peak position were found. With low overall sample Na content, the lattice parameters of the NLZ perovskite phase remained unchanged, corresponding to our aforementioned results where hot sintering-induced overall Na deficiency resulted in pyrochlore phase formation rather than a shift in the NLZ perovskite phase composition and peak position in NLZ-N0.5. These results suggest a narrow (negligible) compositional width for the NLZ perovskite phase in terms of the cation ratio.

4.1.3 NLZ-N0.5-Nb0.05: targeting Na vacancies by donor doping. As a third approach, to further investigate the effect of Na stoichiometry on the NLZ perovskite phase, 5% of Nb was doped onto the B-site in NLZ-N0.5 using the same procedure with the Pechini method; we will abbreviate this composition as NLZ-N0.5-Nb0.05. A decrease in lattice parameters in the NLZ perovskite phase was observed as expected, with Nb^{5+} (0.64 Å) having a smaller ionic radius compared to Zr^{4+} (0.72 Å).[45] With the addition of Nb^{5+}, $Nb^{\cdot}_{Zr}$ is introduced into the NLZ perovskite phase, as Nb has been shown to occupy the B-site in both lead barium zirconate (PBZ) and lead barium zirconate titanate (PBZT) perovskite systems.[47,48] In principle, with the introduction of the $Nb^{\cdot}_{Zr}$ donor, the concentration of positively charged defects such as $v^{\cdot\cdot}_{O}$ and $h^{\cdot}$ may be suppressed, whereas the concentration of negatively charged defects such as v'_{Na} and e'

may be increased in the NLZ perovskite phase.[49] The goal here was ionic compensation with $[v'_{Na}] \approx [Nb^{\bullet}_{Zr}]$ resulting in negligible oxygen ion and electronic charge-carriers. XRD showed that 5% of Nb doping in NLZ-N0.5 resulted in formation of 11.9 wt% pyrochlore phase. This result suggests that the donor doping induced Na deficiency in the sintered sample, but the NLZ perovskite phase does not tolerate many v'_{Na} within the structure. Therefore all three approaches to create v'_{Na} to improve the Na-ion conductivity resulted in secondary phase formation when Na-deficiency was achieved, raising the issue of how the compositional width of the perovskite thermodynamic stability region compares to that of the LLTO parent compound, which readily accommodates Li deficiency.

4.1.4 Thermodynamic stability and defect formation enthalpy of $Na_{0.5}La_{0.5}ZrO_3$. To analyze the thermodynamic stability of $Na_{0.5}La_{0.5}ZrO_3$, we used density functional theory to obtain phase diagrams and assess the possibility of off-stoichiometry. Thermodynamic stability was determined by obtaining the reaction decomposition energies for $Na_{0.5}La_{0.5}ZrO_3$ to other possible competing compounds in the chemical phase space. The possible competing compounds in the La–Na–Zr–O quaternary space were extracted from Materials Project,[50] and only compounds within 40 meV per atom of the convex hull were included in our analysis. These competing compounds are NaO, Na_2O, $La_2Zr_2O_7$, $NaLaO_2$, and ZrO_2. For $Na_{0.5}La_{0.5}ZrO_3$, we simulated a double perovskite structure with an alternating, ordered arrangement of La and Na on the perovskite A-site as shown in Fig. 9.

Different thermodynamic environments were accommodated by the set of chemical potentials μ_j for each element (j = La, Na, Zr, O). We referenced the chemical potential of each species to its corresponding chemical potential in the elemental phase $\mu_j = \mu j^0 + \Delta\mu_j$. The standard formation enthalpy ΔH_f of $Na_{0.5}La_{0.5}ZrO_3$ represents the energy to form the compound from its constituent elemental phases[51,52] and is given by,

$$\Delta H_{Na_{0.5}La_{0.5}ZrO_3} = 0.5\Delta\mu_{Na} + 0.5\Delta\mu_{La} + \Delta\mu_{Zr} + 3\Delta\mu_0 \quad (6)$$

For stability, it must not be favorable for the compound to decompose to either (i) a pure elemental phase or to (ii) a multi-species competing compound.[51] The first condition imposes the constraint that $\Delta\mu_j \leq 0$ for each element. The second condition imposes an additional constraint for each competing compound. For example, to avoid decomposition of $Na_{0.5}La_{0.5}ZrO_3$ to the competing phase NaO, the condition

$$\Delta\mu_{Na} + \Delta\mu_0 \leq \Delta H_{NaO} \quad (7)$$

must hold. If $\Delta H_{NaO} \leq \Delta H_{Na_{0.5}La_{0.5}ZrO_3}$, then NaO will likely form instead of $Na_{0.5}La_{0.5}ZrO_3$. Similar expressions must hold for all other stable competing compounds containing the elements La, Na, Zr, or O.

Fig. 9 shows chemical potential and compositional phase diagrams for two values of the oxygen chemical potential that correspond to different temperatures: (i) $T = 24$ °C, $P = 1$ atm and (ii) $T = 1400$ °C, $P = 1$ atm. DFT calculations reveal a very small stability region for stoichiometric $Na_{0.5}La_{0.5}ZrO_3$ located near the top of the phase diagram, corresponding to a region of relatively high sodium and low lanthanum chemical potential. This suggests that $Na_{0.5}La_{0.5}ZrO_3$ will favor forming under sodium rich and lanthanum poor conditions and therefore will likely have difficulty forming a sodium deficient structure of $Na_{0.5}La_{0.5}ZrO_3$. As Fig. 9(a) and (c) show, under sodium poor conditions, the thermodynamic stability region is limited by the formation of pyrochlore $La_2Zr_2O_7$ and ZrO_2. Thus, these phase diagram results corroborate the experimental findings that this double perovskite crystal structure may not accommodate sodium-deficient compositions, and that zirconia and the pyrochlore form in sodium-poor environments. The main difference between the two oxygen environments in Fig. 9 is the upper phase boundary, which is limited by NaO at room temperature but by Na_2O at high temperature.

Fig. 9(b) and (d) show composition phase diagrams corresponding to the chemical potential phase diagrams in Fig. 9(a) and (c) respectively. Each shaded plane represents a base of an Alkemade tetrahedron that represents a four-phase equilibrium between $Na_{0.5}La_{0.5}ZrO_3$, O_2, and two other compounds. At $T =$ 24 °C, there are three possible four-phase equilibria: one with NaO and ZrO_2, one with NaO and $La_2Zr_2O_7$, and one with $La_2Zr_2O_7$ and ZrO_2. At $T = 1400$ °C, there are four possible four-phase equilibria: with Na_2O and ZrO_2, with Na_2O and $NaLaO_2$, with $NaLaO_2$ and $La_2Zr_2O_7$, and with $La_2Zr_2O_7$ and ZrO_2.

Using the thermodynamic stability diagrams, we estimated the energy needed to introduce $2v'_{Na} + La^{\bullet\bullet}_{Na}$, two sodium vacancies adjacent to a $La^{\bullet\bullet}_{Na}$ antisite defect. This sodium deficient defect complex was considered because it retains charge neutrality based on ionic compensation. We introduced one $2v'_{Na} + La^{\bullet\bullet}_{Na}$ defect in a 40-atom supercell of $Na_{0.5}La_{0.5}ZrO_3$ and determined the defect formation energy according to

$$\Delta E_f = (E_D - E_{host}) + 3\mu_{Na} - \mu_{La} \quad (8)$$

where E_D and E_{host} are respectively the computed energies of the defect-containing and perfect supercells. Using chemical potentials corresponding to the center of the thermodynamic stability region in Fig. 9(a), the formation energy is found to be $\Delta E_f = 2.63$ eV, extremely high for an ionic conductor. For comparison, a recent study in defect chemistry of the non-stoichiometric superionic conductor LGPS discovered the formation energy of a lithium vacancy to be on the order of 0.1 eV.[53] According to Boltzmann statistics, a ΔE_f of 2.63 eV would correspond to a defect concentration of 7.1×10^{-24} per cm^3 at room temperature.

In summary, with Na being a relatively volatile element at high temperatures, Na evaporation is a limiting factor when it comes to selecting sintering conditions in NLZ. Perovskite zirconates are known to have poor sinterability, making it very difficult to densify under lower sintering temperatures. In addition to this kinetic limitation, we have also shown that the NLZ perovskite phase, unlike LLTO, does not accommodate significant Na deficiency regardless of how that deficiency was introduced—by sintering temperature, different starting Na stoichiometry and Na : La ratio, or Nb donor doping. Simulations also demonstrated the high formation enthalpy of the Na

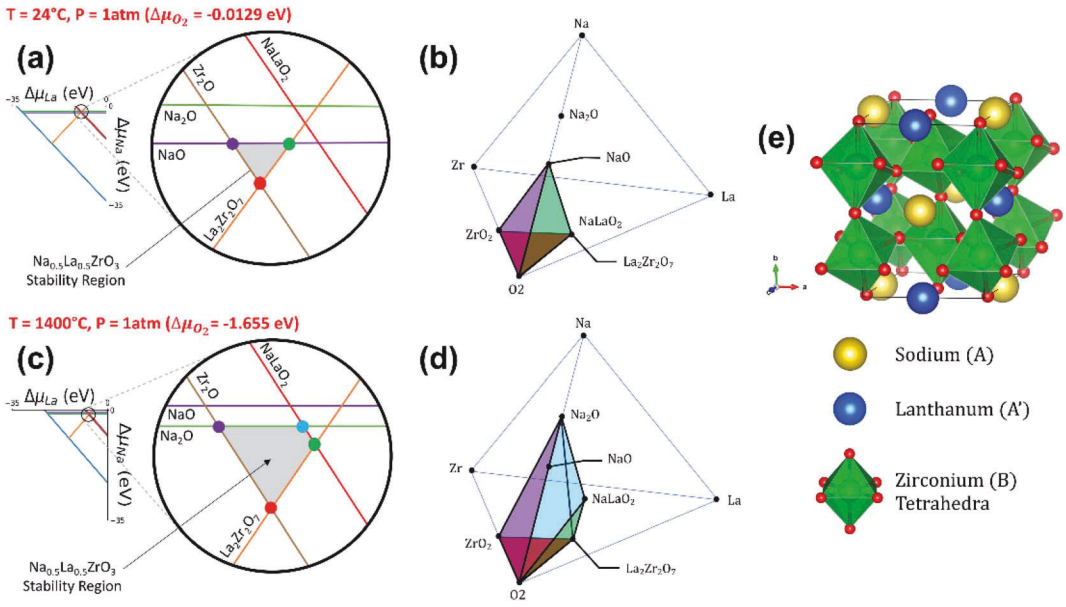

Fig. 9 (a) Calculated chemical potential phase diagram for $Na_{0.5}La_{0.5}ZrO_3$ at room temperature (24 °C). Horizontal and vertical axes correspond to chemical potentials of La and Na respectively. The chemical potential of O_2 is fixed by the corresponding temperature and pressure. The purple, green, and red points in the circular schematic represent four phase equilibria between the intersecting competing compound lines, $Na_{0.5}La_{0.5}ZrO_3$, and O_2. (b) The corresponding composition phase diagram at room temperature. The colors of the shaded planes correspond to the points in the chemical potential phase diagram in part (a). (c) Chemical potential and (d) composition phase diagrams at 1400 °C. (e) Double perovskite crystal structure of $Na_{0.5}La_{0.5}ZrO_3$.

vacancy when generated by a La anti-site defect. As a result of these thermodynamic and kinetic factors, it is challenging to achieve simultaneously high density and phase purity with NLZ. Moreover, the barriers to achieving density and Na deficiency may limit the ionic conductivity of the perovskite.

4.2 Chemo-mechanical and defect engineering: NLBZ-N*x*

The second pillar of our strategy to create Na-ion conducting perovskites was to apply chemo-mechanical engineering to chemically stretch the LLTO starting lattice to accommodate the larger Na-ion that replaces Li. Increasing conductivity and decreasing activation energy have been reported in some Na-ion conductors when their lattice parameters are expanded.[54,55] We initially enlarged the lattice by replacing the B-site Ti with larger Zr. To further enlarge to the conduction channels of NLZ systems, Ba was partially introduced on the A sites, making the composition NLBZ-N*x* ($Na : La : Ba : Zr = x : 1/3-1/3x : 0.5 : 1$ $(0 < x \leq 0.25)$), with Ba occupying half of the A sites. In addition to potentially expanding conduction channels and lowering the activation energy, we also hypothesized that the inclusion of the larger Ba^{2+} (1.61 Å) could increase the stability of the perovskite structure, thereby allowing greater A-site deficiency. Concomitant with this chemo-mechanical engineering strategy, we also pursued similar defect engineering tactics as above to induce Na deficiency (heat treatment, varying Na : La ratio), with the goal of enhancing v'_{Na} formation in the perovskite phase. In the following sub-sections, we interpret the phase composition results for NLBZ-N*x*, with particular emphasis on perovskite lattice dilation and A-site deficiency.

4.2.1 NLBZ-N0.25: chemical expansion. In the NLBZ-N0.25 starting stoichiometry, the composition is stoichiometric, and no initial A-site deficiency is expected; however the impact of the 50% Ba A-site substitution on perovskite symmetry/stability and lattice expansion is of interest. XRD revealed that a reaction occurred during prolonged sintering. The as-calcined powders initially formed two perovskite phases with diffuse peaks. These initial XRD patterns corresponded to those in the database for $BaZrO_3$ and $Na_{0.5}La_{0.5}ZrO_3$. After sintering at 1000 °C for 24 h, the peak positions of the $BaZrO_3$ phase shifted to higher angles (the lattice contracted), while those for the $Na_{0.5}La_{0.5}ZrO_3$ phase shifted to lower angles (the lattice expanded); *i.e.*, they moved closer together, suggesting A-site cation interdiffusion between the two phases. Further heat treatment at 1000 °C for 48 h resulted in little change. Two different perovskite phases were still discernable and not fully reacted at this temperature, while the slight increase in $La_2Zr_2O_7$-like pyrochlore phase can be attributed to prolonged sintering time and likely Na loss.

Sintering at 1200 °C for 6 h resulted in a full reaction between the two initial perovskite phases. XRD analysis of this new phase, $Na_{0.25}La_{0.25}Ba_{0.5}ZrO_3$, revealed peak intensity ratios comparable to $BaZrO_3$, with peak positions falling between those of the original $BaZrO_3$ and $Na_{0.5}La_{0.5}ZrO_3$ phases. However, there was a peak shape difference. Analysis of our synchrotron data (Fig. S1 and S2†) suggests that $Na_{0.25}La_{0.25}Ba_{0.5}ZrO_3$ was in a cubic perovskite phase, whereas $Na_{0.5}La_{0.5}ZrO_3$ was orthorhombic with more peak splitting.[35,37] This result – both the lattice enlargement and increase in symmetry as Ba is substituted on the A-site – is consistent with a simple tolerance factor analysis. The ability of a certain ABO_3 composition to

form the perovskite phase stably has been described empirically through the Goldschmidt tolerance factor, on the basis of the ionic radii. Values close to 1 indicate a more ideal cubic perovskite may be formed, and the perovskite phase tends to form for values in the range 0.71–1.05; values near the edges of this range might indicate structures with less ability to maintain the perovskite structure during stoichiometric changes. NLBZ has a calculated tolerance factor of 0.9648, whereas for NLZ it is 0.9256. The cell volume of $Na_{0.25}La_{0.25}Ba_{0.5}ZrO_3$ was increased to 71.23 Å^3, relative to the $Na_{0.5}La_{0.5}ZrO_3$ cell volume of 67.32 Å^3. The relative density was measured to be 44.51% due to the poor sinterability of perovskite zirconates at low temperatures. The barely discernable ~2 wt% $La_2Zr_2O_7$-like pyrochlore phase present could be due to an error in cation ratios during the modified Pechini synthesis process or slight Na loss during sintering.

Heat treatment at a higher temperature of 1400 °C for 6 h achieved higher density, at the expense of significant Na loss—consistent with the behavior of the NLZ system. The density was measured to be 63.3%, and the fraction of the $La_2Zr_2O_7$-like pyrochlore phase increased to 9.36 wt% as expected. The peak positions of the NLBZ perovskite phase sintered at 1400 °C for 6 h were shifted to lower angles compared to NLBZ-N0.25-(1200C 6hr), indicating an increase in lattice parameters from $a = 4.145$ Å to $a = 4.158$ Å with the higher sintering temperature. The lattice expansion may be caused by Na vacancies on the A-site in the NLBZ perovskite phase, with possible charge compensation from oxygen vacancies or holes, for example, as discussed in Sec. 4.1.1 above.[56–58] Note that ionized oxygen vacancies or holes by themselves are likely to contract the lattice,[57,59] so any expansion in this case would be due to the v'_{Na}. A-site vacancies are usually larger compared to occupied A-sites.[58] (Based on the invariant conductivity *vs.* pO_2 behavior, a high concentration of mobile holes is actually ruled out.) Hydration could also enlarge lattice parameters *via* proton incorporation, but the measurements were performed under identical conditions after sample storage in dry environments, suggesting that the samples sintered at different temperatures did not have different proton concentrations as the primary reason underlying the strain. This lattice expansion could therefore indicate that A-site deficient NLBZ is stable and possible to synthesize, but the degree of A-site deficiency or A-site composition remains unknown. Na has the highest vapor pressure of any of the cations (including Ba) for this composition, so it is the most likely candidate to cause cation vacancies during heat treatments.

4.2.2 NLBZ-N0.125: exceeding limit of Na deficiency. Following the same procedure on NLZ systems, non-stoichiometric NLBZ powders were synthesized (NLBZ-N*x* powders, $x \neq 0.25$) with the goal of stabilizing more v'_{Na}. First, NLBZ-N0.125 starting powders were pressed and sintered at 1200 °C for 6 h. XRD shows that the NLBZ-N0.125-(1200C 6hr) pellet is composed of two phases: primarily perovskite phase, with 15.4 wt% of the pyrochlore-like phase. The peak positions of the perovskite phase in the NLBZ-N0.125-(1200C 6hr) pellet line up well with the peaks in NLBZ-0.25-(1400C 6hr) pellet. This agreement suggests that the NLBZ perovskite phase in NLBZ-0.125 pellet was indeed A-site deficient, and the same limit of A-site deficiency was reached in the perovskite phases within both NLBZ-N0.25-(1400C 6hr) and NLBZ-N0.125-(1200C 6hr) samples. Going beyond this limit in the overall sample composition results in secondary phase formation.

In summary, the NLBZ perovskite phase may have more tolerance for Na deficiency compared to NLZ. It is possible that the Ba^{2+} substitution in NLBZ indeed help stabilize the perovskite phase, allowing some degree of v'_{Na} as opposed to NLZ. Na-deficient NLBZ perovskite phase could be synthesized. It is, however, still challenging to synthesize NLBZ without any $La_2Zr_2O_7$-like pyrochlore phase either *via* higher sintering temperatures or lower initial Na stoichiometries. Similar to NLZ, NLBZ is also difficult to densify using conventional sintering methods. The microstructure is porous, as can be seen in the SEM images presented in Fig. 2. Previous research has shown that the minor presence of an impurity phase does not impact electrical conductivities significantly in lithium conductors and oxide ion conductors.[60–62] Impedance measurements can thus be performed on NLBZ-N0.25-(1200C 6hr) with minor pyrochlore phase with necessary corrections, assuming the pyrochlore phase to be completely insulating.

4.3 Electrical behavior: impact of stoichiometry, lattice size, and humidity

4.3.1 Electrical properties of NLZ-N0.5-(1200C 6hr). In dry environments, EIS and DC polarization measurements on NLZ-N0.5-(1200C 6hr) under different pO_2 suggested that sodium ions were the primary carrier species, with negligible electronic transference number (t_{elec}) and low oxygen-ion transference number (t_O). More discussion on transference numbers can be seen in ESI Sec. 3.† The ionic conductivity was lower than that of LLTO; this difference can at least partially be attributed to the low concentration of v'_{Na} within the $Na_{0.5}La_{0.5}ZrO_3$ perovskite phase as discussed in the previous sections. With a high concentration of Na sites occupied, sodium ion conduction was likely impeded without available sites to hop into.

To determine how protons affect the total conductivity in gas atmospheres containing humidity, electrical measurements for the same sample were performed in humid conditions also under different pO_2 at various temperatures. In the study of ionic conductors, it is important to separate the potential contribution of protons; otherwise, the source of the total conductivity could be mis-identified. Certain oxygen-deficient oxides have been shown to be able to incorporate protons in humid environments *via* oxygen vacancies,[63,64] with water dissociating into oxygen vacancy and lattice oxygen sites being one possible mechanism as seen in eqn (9):

$$H_2O + v''_O + O^\times_O \rightarrow 2(OH)^\bullet_O \quad (9)$$

Additionally, some Li-ion conductors have been shown to undergo mobile cation exchange with protons in acidic media or humid conditions, suggesting the possibility of proton diffusion/intercalation along similar pathways to Li.[65–67] With protons incorporated into the NLZ-N0.5-(1200C 6hr) in humid

environments, a decrease in conductivities was observed at low temperatures (300–400 °C) in both $pO_2 = 10^{-5}$ atm and $pO_2 = 1$ atm. This decrease might be attributed to the presence of protons disrupting Na transport. Similar behavior has been seen in Li conductors, where water exposure and proton formation have been shown to decrease conductivity in LLZO, as a result of protons being in the pathways of lithium transport and disrupting the migration process.[68] Alternatively, the lower conductivity in humid conditions could indicate sluggish proton transport along the Na pathways. When the measurement temperature was raised to the higher temperature range (400–600 °C), conductivities were identical in all conditions (*e.g. vs.* pO_2, humidity). We attribute this agreement to a dehydration reaction where protons were removed from the lattice, causing the sample to be dehydrated even under humid conditions, with the effect of protons diminished. From impedance measurements at different temperatures, it can be inferred that the dehydration reaction occurred above 400 °C for NLZ-N0.5-(1200C 6hr), making transport properties similar for both dry and humid conditions above 400 °C. Dehydration thermodynamics vary depending on the composition of oxide proton conductors.[69–71]

4.3.2 Electrical properties of NLBZ-N0.25-(1200C 6hr). In dry environments, similar electrical behavior was observed in NLBZ-N0.25-(1200C 6hr) compared to NLZ, with sodium-ions being the main carrier species; however, in humid conditions, conductivities were independent of pO_2 and higher compared to dry conditions for any temperatures between 300 °C and 600 °C, suggesting that the sample remains hydrated up to 600 °C under humid conditions. Protons have been shown to act as additional carriers and give an increase in conductivity in their hydrated state in certain compositions. For instance, $Ba_4In_2Zr_2O_{11}$-based proton conductors showed higher conductivity when hydrated.[72] It can thus be inferred that NLBZ-N0.25-(1200C 6hr) was able to stay hydrated in the range of 300–600 °C, forming protons as additional conducting species, and possibly transported *via* the Grotthuss mechanism. This opposite behavior compared to NLZ-N0.5-(1200C 6hr) may be attributed to the presence of Ba^{2+}. Barium containing zirconates have been known to be able to incorporate water and conduct protons more easily due to their low Brønsted basicity.[73,74] It can also be noted that the conductivity at higher temperature started to deviate from Arrhenius behavior above 400 °C, which might be explained by some degree of dehydration. As the temperature increased, the magnitude of increase in conductivity in humid environments *vs.* dry conditions decreased. This suggests that proton concentration decreased with increasing temperature. Yttrium-doped barium zirconates have been shown to exhibit similar proton conduction behavior, where dehydration and deviation of conductivity from Arrhenius behavior was observed at higher temperatures.[75,76]

To summarize, proton formation has opposite effects on conductivities of NLZ-N0.5-(1200C 6hr) *vs.* NLBZ-N0.25-(1200C 6hr), with decreased conductivities at low temperatures (<400 °C) for the former, and increased conductivities across the temperature range (300–600 °C) for the latter. The difference of conductivities *vs.* dry conditions in certain temperature ranges would suggest that the introduction of Ba into the perovskite structure significantly modified proton formation and the dehydration process, with the Ba-containing composition being able to incorporate protons over a larger temperature range. Our results suggest that protons were blocking to Na transport and/or poorly mobile in the composition without Ba; oppositely, protons were mobile and acted as an extra carrier species in the composition with Ba.

4.3.3 Comparison between NLZ-N0.5-(1200C 6hr), NLBZ-N0.25-(1200C 6hr), NLBZ-N0.125-(1200C 6hr), and NLZ-N0.5-(SPS+1000C 24hr). The conductivities of NLZ-N0.5-(1200C 6hr) and NLBZ-N0.25-(1200C 6hr) are shown in Fig. 8; only dry conditions are compared here without the effect of protons. With both compositions having larger cell volume (Sec. 4.2.1) compared to $Na_{0.42}La_{0.525}TiO_3$ (58.08 Å^3),[15] NLZ and NLBZ exhibited higher σ_h and lower E_A compared to unexpanded $Na_{0.42}La_{0.525}TiO_3$,[15] as seen in Fig. 8. This significant difference suggests that the transport of Na ions can be effectively enhanced within ABO_3 perovskite slabs in LLTO-type perovskites by enlarging of the lattice *via* a chemo-mechanical engineering approach. Moreover, the conductivity of NLZ is also comparable with that of $NaNbO_3$ reported by Gouget *et al.*,[31] despite only having half the carrier concentration compared to $NaNbO_3$. NLZ also exhibits higher Na transference numbers than $NaNbO_3$. Even higher conductivity can be found in the densest sample fabricated using SPS, NLZ-N0.5-(SPS+1000C 24hr). While the exact reason for this difference is not known, a few possible contributors exist: (a) SPS may modify the defect chemistry; (b) there may be some inaccuracy in the porosity correction applied to the more porous samples, given imperfectly spherical grains and pores; (c) grain-to-grain connections may be less constricted in the denser sample; and (d) the grain sizes were different between NLZ-N0.5-(SPS+1000C 24hr) NLZ-N0.5-(1200C 6hr). However, overall, the conductivities of NLZ and NLBZ are still considerably lower compared to known Na super-ionic conductors like β”-alumina[6] and NASICONs.[7] More comparison of conductivity with other perovskite Na-ion conductors (including RP phases) can be found in Sec. 4 in ESI.†

The total conductivity of NLBZ-N0.25-(1200C 6hr) is lower than that of NLZ-N0.5-(1200C 6hr), which can be explained by the lower concentration of Na. The conductivity pre-factor includes the carrier concentration term, with Na ion concentration in NLBZ-N0.25-(1200C 6hr) being only half that of NLZ-N0.5-(1200C 6hr). Experimentally, the conductivity pre-factor was decreased almost in half, resulting in a decrease in total conductivity. Because of the larger lattice parameter in NLBZ-N0.25-(1200C 6hr), larger conduction channels are also expected, which could result in a decrease in activation energy. However, our results showed a very slight increase in activation energy, which may be within the margin of error. Although rare, this counter-intuitive effect has also been seen in other cation conductors, where enlarged conduction channels actually led to a decrease in ionic conductivity.[77] In addition, some researchers have suggested that superionic conductors have optimal “percolation radii” for mobile cations, and the diffusion channel should not be too small or too large.[78,79] In the case of NLBZ-N0.25-(1200C 6hr), the conduction channel may have

been too large, starting to fall out of the range of the optimal percolation radius. Nonetheless, other studies have observed no limit to the benefit of tensile strain for conductivity in cation conductors.[80–84] In the present work, an alternative factor that may account for the limited benefit from the larger lattice relates to the local interactions: it is possible that the introduction of Ba resulted in a different bonding environment for Na, where modified coulombic interactions between Na and O cause Na–O bonds to become stronger, countering the effect of the enlarged conduction channels.[77] In other words, chemo-mechanical engineering should be applied carefully, considering the balance of macroscopic lattice strain and local inhomogeneous atomic interaction effects.[34]

Another interesting fact to be noted here is that the Nyquist plots for both NLZ-N0.5-(1200C 6hr) and NLBZ-N0.25-(1200C 6hr), as seen in Fig. 5, showed that there was only one arc. DRT analysis also showed that there was only one process in all the spectra (Fig. S5(d)†) under different measurement temperatures in dry conditions, where additional carriers such as protons and Ag are excluded. (The effect of Ag and Pt electrodes can be seen in Sec. 2 in ESI.†) Although NLZ-N0.5-(1200C 6hr) and NLBZ-N0.25-(1200C 6hr) were polycrystalline as can be seen in the SEM images, the impedance spectra did not show different contributions from the grain core and the grain boundaries. Three hypotheses are proposed here to explain this phenomenon: (1) the grain boundaries are not significantly blocking to cation transport in the range of 300–600 °C, such that the response represents the bulk. For some cation conductors, grain boundaries are blocking at low temperatures but cease to be significantly blocking at high temperatures due to their higher activation energies, and the impedance spectra correspondingly can show a transition from dual to single arc behavior, with a shrinking of the grain boundary arc, as temperature increases;[85] or (2) the relaxation time of the grain core and the grain boundaries were almost identical, making them indistinguishable; or (3) the conduction primarily takes place in the vicinity of the surfaces/grain boundaries in the porous microstructure, resulting in a fast path through the microstructure and only one process visible in the impedance spectra. On the basis of the measured dielectric permittivities corresponding to this impedance arc (see Sec. 3.2.1), we think that hypothesis (1) is reasonable.

Finally, the conductivity of NLBZ-N0.125-(1200C 6hr) was also measured with Au electrodes for comparison. The pyrochlore phase was assumed to be completely insulating in the correction process. The conductivity of the perovskite phase in NLBZ-N0.125-(1200C 6hr) is much lower compared to the other samples, as seen in Fig. 8. It is likely that the significant decrease in conductivity was a result of the further decrease in Na-ion concentration.

5 Summary and conclusion

In this work, $Na_{0.5}La_{0.5}ZrO_3$ and $Na_{0.25}La_{0.25}Ba_{0.5}ZrO_3$ were synthesized using a modified Pechini method as a route to emulate the perovskite structure of the superionic lithium conductor LLTO. In order to accommodate larger Na *vs.* Li ions, the lattices were expanded with the substitution of Zr^{4+} and Ba^{2+} on the B- and A-sites of the original LLTO perovskite structure, respectively. In addition to this strain engineering approach, we attempted to introduce v'_{Na} systematically to improve the Na-ion conductivity, by long/hot sintering, sub-stoichiometric Na : La and A : B site ratios, and donor doping. Although each of these three methods charge-compensates for v'_{Na} through different positively-charged defect species, our XRD results indicated a common phenomenon: the NLZ structure could not accommodate significant A-site deficiency, making it difficult to enhance the ionic conductivity without higher v'_{Na} concentrations. On the other hand, the Ba-containing NLBZ appeared to accommodate some degree of A-site deficiency, though the minor formation of electrically insulating impurity phases could not be avoided when the Na content further decreased beyond this limit. The poor sinterability typical of zirconates made it challenging to densify NLZ and NLBZ without the loss of Na because of its volatility; as a result, impurity phases tended to form when pursuing high densities using conventional methods. On the other hand, although the sample was mechanically less robust, higher density and minimal Na loss could be achieved by an advanced sintering technique like SPS.

In terms of electrical properties, both $Na_{0.5}La_{0.5}ZrO_3$ and $Na_{0.25}La_{0.25}Ba_{0.5}ZrO_3$ showed higher conductivity and lower activation energy compared to unexpanded $Na_{0.42}La_{0.525}TiO_3$,[15] suggesting that the lattice enlargement effectively boosted the mobility of Na ions. The conductivity of $Na_{0.5}La_{0.5}ZrO_3$ is also comparable with $NaNbO_3$,[31] despite only having half the carrier concentration and a higher Na transference number. Promisingly, the SPS-treated sample had even higher conductivity than those sintered conventionally. $Na_{0.5}La_{0.5}ZrO_3$ exhibited higher ionic conductivity compared to $Na_{0.25}La_{0.25}Ba_{0.5}ZrO_3$, which can be attributed to the lower Na-ion concentration of the latter composition. While the lattice enlargement of the new $Na_{0.5}La_{0.5}ZrO_3$ relative to previously-reported $Na_{0.42}La_{0.525}TiO_3$ (ref. 15) helped to decrease the conductivity activation energy, counter-intuitively, the expected further enlarged conduction channels of $Na_{0.25}La_{0.25}Ba_{0.5}ZrO_3$ *via* partial substitution of Ba^{2+} on the A-site resulted in a similar E_A compared to $Na_{0.5}La_{0.5}ZrO_3$. It is possible that this result stemmed from a deviation from optimal conduction channel size and/or a difference in Na bonding environment. AC impedance spectroscopy measurements in dry environments under different pO_2s resulted in no change in total conductivity, suggesting negligible electronic conductivity for both compositions, making them suitable for electrolyte applications. Moreover, DC polarization experiments using reversible oxygen electrodes (porous gold) confirmed that oxygen ion conductivities were also low for both compositions.

The effect of humidity was also investigated, with incorporated protons lowering the total ionic conduction in $Na_{0.5}La_{0.5}ZrO_3$ in the low temperature range (300–400 °C), and protons improving ionic transport in $Na_{0.25}La_{0.25}Ba_{0.5}ZrO_3$ across the full temperature range (300–600 °C). The introduction of Ba^{2+} had a significant impact on the hydration/dehydration process; the proton transport properties and their interaction with Na-ions were also altered appreciably.

Taken together, these results indicate that while strain and defect engineering are reasonable strategies to turn a Li-ion conductor into new Na-ion conducting compositions, the intrinsic limitations of a new composition – the kinetics of cation interdiffusion, cation vapor pressure, thermodynamic stability bounds, and point defect formation enthalpies – may conspire to limit the electrical performance of the resulting product, particularly using conventional sintering approaches close to thermodynamic equilibrium. As a result, the conductivities of NLZ and NLBZ are likely too low in bulk ceramic, equilibrium form, for room temperature batteries. However, given their stability at high temperatures in a wide range of pO_2, they could still be of interest for higher temperature electrochemical cells used in large-scale stationary storage. Furthermore, because the new compositions in the present study are almost pure Na-ion conductors with low electronic conductivity in dry conditions, they may be worth synthesizing through alternative means. Non-equilibrium routes, such as energetic thin film growth, may enhance relative density and quench-in metastable defect concentrations in future work. We also emphasize the importance of verifying the nature of the charge-carrying species in new solid electrolytes, given possible contributions from anions, electrons, holes, and protons in addition to the desired mobile cation charge-carrier, and the importance of working with suitably inert electrodes.

Author contributions

Yu-Ying Lin: formal analysis, investigation, validation, visualization, writing – original draft, writing – review & editing, project administration. William J. Gustafson: formal analysis, visualization, writing – original draft, writing – review & editing. Shannon E. Murray: investigation, writing – original draft. Daniel P. Shoemaker: resources, supervision, funding acquisition. Elif Ertekin: resources, methodology, supervision, writing – review & editing, funding acquisition. Jessica A. Krogstad: conceptualization, methodology, resources, supervision, writing – review & editing, project administration, funding acquisition. Nicola H. Perry: conceptualization, methodology, resources, supervision, writing – review & editing, project administration, funding acquisition.

Conflicts of interest

The authors declare that they have no known competing financial interests or personal relationships that could have appeared to influence the work reported in this paper.

Acknowledgements

This material is primarily based upon work supported by the US Army CERL W9132T-19-2-0008 (to E. E., J. A. K. and N. H. P., also supporting Y. Y. L.). D. P. S. acknowledges research support by the Army Research Office under Grant Number W911NF-17-1-0142. S. E. M. acknowledges support from the National Science Foundation Graduate Research Fellowship Program under Grant No. DGE1144245. XRD, SEM, and sputter coating were carried out in the Materials Research Laboratory Central Research Facilities, University of Illinois. The authors also acknowledge the use of XRD instrumentation supported by NSF through the University of Illinois Materials Research Science and Engineering Center DMR-1720633. Use of the Advanced Photon Source at Argonne National Laboratory was supported by the U. S. Department of Energy, Office of Science, Office of Basic Energy Sciences, under Contract No. DE-AC02-06CH11357. The authors would like to thank Dr Charles Smith and Dr Nathan Madden (University of Illinois at Urbana-Champaign) for their help with using spark plasma sintering as an alternative route to densify the pellet.

References

1 A. M. Skundin, T. L. Kulova and A. B. Yaroslavtsev, *Russ. J. Electrochem.*, 2018, **54**, 113–152.
2 A. Ponrouch, D. Monti, A. Boschin, B. Steen, P. Johansson and M. R. Palacín, *J. Mater. Chem. A*, 2015, **3**, 22–42.
3 Z. Zhang, Y. Shao, B. Lotsch, Y.-S. S. Hu, H. Li, J. Janek, L. F. Nazar, C.-W. W. Nan, J. Maier, M. Armand and L. Chen, *Energy Environ. Sci.*, 2018, **11**, 1945–1976.
4 K. B. Hueso, M. Armand and T. Rojo, *Energy Environ. Sci.*, 2013, **6**, 734.
5 Z. Zhang, Y. Shao, B. Lotsch, Y.-S. Hu, H. Li, J. Janek, L. F. Nazar, C.-W. Nan, J. Maier, M. Armand and L. Chen, *Energy Environ. Sci.*, 2018, **11**, 1945–1976.
6 X. Lu, G. Xia, J. P. Lemmon and Z. Yang, *J. Power Sources*, 2010, **195**, 2431–2442.
7 N. Anantharamulu, K. Koteswara Rao, G. Rambabu, B. Vijaya Kumar, V. Radha and M. Vithal, *J. Mater. Sci.*, 2011, **46**, 2821–2837.
8 Y. Sun, P. Guan, Y. Liu, H. Xu, S. Li and D. Chu, *Crit. Rev. Solid State Mater. Sci.*, 2019, **44**, 265–282.
9 C. H. Chen and J. Du, *J. Am. Ceram. Soc.*, 2014, **98**, 534–542.
10 P. Ramakrishnan, H. Kwak, Y. H. Cho and J. H. Kim, *ChemElectroChem*, 2018, **5**, 1265–1271.
11 K. Toda, Y. Kameo, S. Kurita and M. Sato, *J. Alloys Compd.*, 1996, **234**, 19–25.
12 A. A. Petrov, N. A. Melnikova, A. V. Petrov, O. I. Silyukov, I. V. Murin and I. A. Zvereva, *Ceram. Int.*, 2017, **43**, 10861–10865.
13 S.-H. Byeon, K. Park and M. Itoh, *J. Solid State Chem.*, 1996, **121**, 430–436.
14 A. Rivera, C. León, J. Santamaría, A. Várez, O. V'yunov, A. G. Belous, J. A. Alonso and J. Sanz, *Chem. Mater.*, 2002, **14**, 5148–5152.
15 A. I. Ruiz, M. L. López, C. Pico and M. L. Veiga, *J. Solid State Chem.*, 2002, **163**, 472–478.
16 S. Gates-Rector and T. Blanton, *Powder Diffr.*, 2019, **34**, 352–360.
17 D. A. G. Bruggeman, *Ann. Phys.*, 1935, **416**, 636–664.
18 D. S. McLachlan, M. Blaszkiewicz and R. E. Newnham, *J. Am. Ceram. Soc.*, 1990, **73**, 2187–2203.
19 W. Pabst and E. Gregorová, *J. Eur. Ceram. Soc.*, 2014, **34**, 2757–2766.

20 T. H. Wan, M. Saccoccio, C. Chen and F. Ciucci, *Electrochim. Acta*, 2015, **184**, 483–499.
21 P. Hohenberg and W. Kohn, *Phys. Rev.*, 1964, **136**, B864–B871.
22 W. Kohn and L. J. Sham, *Phys. Rev.*, 1965, **140**, A1133–A1138.
23 G. Kresse and J. Furthmüller, *Phys. Rev. B: Condens. Matter Mater. Phys.*, 1996, **54**, 11169–11186.
24 G. Kresse and J. Furthmüller, *Comput. Mater. Sci.*, 1996, **6**, 15–50.
25 M. Li, T. Utigard and M. Barati, *Metall. Mater. Trans. B*, 2015, **46**, 74–82.
26 S. Jo, *Solid State Ionics*, 2008, **178**, 1990–1997.
27 R. Gu, K. Yu, L. Wu, R. Ma, H. Sun, L. Jin, Y. Xu, Z. Xu and X. Wei, *Ceram. Int.*, 2019, **45**, 8243–8247.
28 K. Yu, Y. Tian, R. Gu, L. Jin, R. Ma, H. Sun, Y. Xu, Z. Xu and X. Wei, *J. Eur. Ceram. Soc.*, 2018, **38**, 4483–4487.
29 S. Lunghammer, D. Prutsch, S. Breuer, D. Rettenwander, I. Hanzu, Q. Ma, F. Tietz and H. M. R. Wilkening, *Sci. Rep.*, 2018, **8**, 11970.
30 K. Kataoka, H. Nagata and J. Akimoto, *Sci. Rep.*, 2018, **8**, 9965.
31 G. Gouget, F. Mauvy, U.-C. Chung, S. Fourcade, M. Duttine, M.-D. Braida, T. Le Mercier and A. Demourgues, *Adv. Funct. Mater.*, 2020, **30**, 1909254.
32 X. Gao, C. A. J. Fisher, T. Kimura, Y. H. Ikuhara, H. Moriwake, A. Kuwabara, H. Oki, T. Tojigamori, R. Huang and Y. Ikuhara, *Chem. Mater.*, 2013, **25**, 1607–1614.
33 H. Moriwake, X. Gao, A. Kuwabara, C. A. J. Fisher, T. Kimura, Y. H. Ikuhara, K. Kohama, T. Tojigamori and Y. Ikuhara, *J. Power Sources*, 2015, **276**, 203–207.
34 Y.-Y. Lin, A. X. Bin Yong, W. J. Gustafson, C. N. Reedy, E. Ertekin, J. A. Krogstad and N. H. Perry, *Curr. Opin. Solid State Mater. Sci.*, 2020, **24**, 100875.
35 M. C. Knapp and P. M. Woodward, *J. Solid State Chem.*, 2006, **179**, 1076–1085.
36 M. C. Knapp, *Investigations into the structure and properties of ordered perovskites, layered perovskites, and defect pyrochlores*, The Ohio State University, 2006.
37 S. García-Martín, E. Urones-Garrote, M. C. Knapp, G. King and P. M. Woodward, *MRS Proc.*, 2008, **1148**, 1148-PP15-05.
38 R. H. Lamoreaux and D. L. Hildenbrand, *J. Phys. Chem. Ref. Data*, 1984, **13**, 151–173.
39 J. Lee and Y. Chiang, *J. Mater. Chem.*, 1999, **9**, 3107–3111.
40 J. Tong, D. Clark, M. Hoban and R. O'Hayre, *Solid State Ionics*, 2010, **181**, 496–503.
41 J. Tong, D. Clark, L. Bernau, A. Subramaniyan and R. O'Hayre, *Solid State Ionics*, 2010, **181**, 1486–1498.
42 I. Kokal, M. Somer, P. H. L. Notten and H. T. Hintzen, *Solid State Ionics*, 2011, **185**, 42–46.
43 M. Kotobuki, K. Kanamura, Y. Sato and T. Yoshida, *J. Power Sources*, 2011, **196**, 7750–7754.
44 S. E. Murray, T. J. Jensen, S. S. Sulekar, Y. Lin, N. H. Perry and D. P. Shoemaker, *J. Am. Ceram. Soc.*, 2019, **102**, 7210–7216.
45 R. D. Shannon, *Acta Crystallogr., Sect. A: Cryst. Phys., Diffr., Theor. Gen. Crystallogr.*, 1976, **32**, 751–767.
46 S. Stramare, V. Thangadurai and W. Weppner, *Chem. Mater.*, 2003, **15**, 3974–3990.
47 B. Fraygola, U. Salazar, A. Biancoli, D. Damjanovic and N. Setter, *Joint IEEE International Symposium on Applications of Ferroelectric and Workshop on Piezoresponse Force Microscopy (ISAF/PFM)*, IEEE, 2013, vol. 4, pp. 89–92.
48 M.-J. Pan, R. J. Rayne and B. A. Bender, *J. Electroceramics*, 2005, **14**, 139–148.
49 C. Slouka, T. Kainz, E. Navickas, G. Walch, H. Hutter, K. Reichmann and J. Fleig, *Materials*, 2016, **9**, 945.
50 A. Jain, S. P. Ong, G. Hautier, W. Chen, W. D. Richards, S. Dacek, S. Cholia, D. Gunter, D. Skinner, G. Ceder and K. A. Persson, *APL Mater.*, 2013, **1**, 011002.
51 S. Chen, J.-H. Yang, X. G. Gong, A. Walsh and S.-H. Wei, *Phys. Rev. B: Condens. Matter Mater. Phys.*, 2010, **81**, 245204.
52 M. Geng and H. Jónsson, *Phys. Chem. Chem. Phys.*, 2019, **21**, 1009–1013.
53 P. Gorai, H. Long, E. Jones, S. Santhanagopalan and V. Stevanović, *J. Mater. Chem. A*, 2020, **8**, 3851–3858.
54 S. Xiong, Z. Liu, H. Rong, H. Wang, M. McDaniel and H. Chen, *Sci. Rep.*, 2018, **8**, 9146.
55 Z. Deng, J. Gu, Y. Li, S. Li, J. Peng, X. Li, J. Luo, Y. Huang, C. Fang, Q. Li, J. Han, Y. Huang and Y. Zhao, *Electrochim. Acta*, 2019, **298**, 121–126.
56 R. Ubic, K. Tolman, K. Chan, N. Lundy, S. Letourneau and W. Kriven, in *Processing and Properties of Advanced Ceramics and Composites V*, 2013, pp. 331–336.
57 D. Marrocchelli, N. H. Perry and S. R. Bishop, *Phys. Chem. Chem. Phys.*, 2015, **17**, 10028–10039.
58 R. Ubic, K. Tolman, K. Talley, B. Joshi, J. Schmidt, E. Faulkner, J. Owens, M. Papac, A. Garland, C. Rumrill, K. Chan, N. Lundy and H. Kungl, *J. Alloys Compd.*, 2015, **644**, 982–995.
59 S. R. Bishop, D. Marrocchelli, C. Chatzichristodoulou, N. H. Perry, M. B. Mogensen, H. L. Tuller and E. D. Wachsman, *Annu. Rev. Mater. Res.*, 2014, **44**, 205–239.
60 S. A. Yoon, N. R. Oh, A. R. Yoo, H. G. Lee and H. C. Lee, *J. Korean Ceram. Soc.*, 2017, **54**, 278–284.
61 S.-L. Zhang, T. Liu, C.-J. Li, S.-W. Yao, C.-X. Li, G.-J. Yang and M. Liu, *J. Mater. Chem. A*, 2015, **3**, 7535–7553.
62 T. Chen, G. F. Harrington, J. Matsuda, K. Sasaki, D. Pham, E. L. Corral and N. H. Perry, *J. Electrochem. Soc.*, 2019, **166**, F569–F580.
63 K. H. Ryu and S. M. Haile, *Solid State Ionics*, 1999, **125**, 355–367.
64 P. Babilo, T. Uda and S. M. Haile, *J. Mater. Res.*, 2007, **22**, 1322–1330.
65 L. Sebastian, R. S. Jayashree and J. Gopalakrishnan, *J. Mater. Chem.*, 2003, **13**, 1400–1405.
66 T. Wei, L. A. Zhang, Y. Chen, P. Yang and M. Liu, *Chem. Mater.*, 2017, **29**, 1490–1495.
67 A. Boulant, P. Maury, J. Emery, J.-Y. Buzare and O. Bohnke, *Chem. Mater.*, 2009, **21**, 2209–2217.
68 Y. Wang and W. Lai, *J. Power Sources*, 2015, **275**, 612–620.
69 C. Zhang, H. Zhao and S. Zhai, *Int. J. Hydrogen Energy*, 2011, **36**, 3649–3657.
70 A. Kruth, *Solid State Ionics*, 2003, **162–163**, 83–91.

71 N. Torino, P. F. Henry, C. S. Knee, S. K. Callear, R. I. Smith, S. M. H. Rahman and S. G. Eriksson, *Solid State Ionics*, 2018, **324**, 233–240.
72 N. A. Tarasova, A. O. Galisheva and I. E. Animitsa, *Russ. J. Electrochem.*, 2019, **55**, 756–761.
73 K. D. Kreuer, *Annu. Rev. Mater. Res.*, 2003, **33**, 333–359.
74 N. Bonanos, *Solid State Ionics*, 2001, **145**, 265–274.
75 Y. Yamazaki, R. Hernandez-Sanchez and S. M. Haile, *Chem. Mater.*, 2009, **21**, 2755–2762.
76 D. Han, N. Hatada and T. Uda, *J. Electrochem. Soc.*, 2016, **163**, F470–F476.
77 T. Krauskopf, S. P. Culver and W. G. Zeier, *Chem. Mater.*, 2018, **30**, 1791–1798.
78 X. He, Q. Bai, Y. Liu, A. M. Nolan, C. Ling and Y. Mo, *Adv. Energy Mater.*, 2019, **9**, 1902078.
79 J. C. Bachman, S. Muy, A. Grimaud, H.-H. Chang, N. Pour, S. F. Lux, O. Paschos, F. Maglia, S. Lupart, P. Lamp, L. Giordano and Y. Shao-Horn, *Chem. Rev.*, 2016, **116**, 140–162.
80 A. Martínez-Juárez, C. Pecharromán, J. E. Iglesias and J. M. Rojo, *J. Phys. Chem. B*, 1998, **102**, 372–375.
81 F. Chen, L. Xu, J. Li, Y. Yang and Q. Shen, *Ionics*, 2020, **26**, 3193–3198.
82 Y. Wang, W. D. Richards, S. P. Ong, L. J. Miara, J. C. Kim, Y. Mo and G. Ceder, *Nat. Mater.*, 2015, **14**, 1026–1031.
83 L. J. Miara, S. P. Ong, Y. Mo, W. D. Richards, Y. Park, J.-M. Lee, H. S. Lee and G. Ceder, *Chem. Mater.*, 2013, **25**, 3048–3055.
84 S. P. Ong, Y. Mo, W. D. Richards, L. Miara, H. S. Lee and G. Ceder, *Energy Environ. Sci.*, 2013, **6**, 148–156.
85 S. Lunghammer, Q. Ma, D. Rettenwander, I. Hanzu, F. Tietz and H. M. R. Wilkening, *Chem. Phys. Lett.*, 2018, **701**, 147–150.

